

1 **Observations of creep of polar firn at different temperatures**

2
3 Yuan Li^{1,3}, Kaitlin Keegan², Ian Baker¹

4 ¹Thayer School of Engineering, Dartmouth College, Hanover, NH, 03755, USA

5 ²Department of Geological Sciences & Engineering, University of Nevada, Reno, Reno, NV,
6 89557, USA

7 ³X-Here (Future ice-based Hydrogen energy & resilient environments) Trek Laboratory
8 (Establishing), Howard Beach, NY, 11414, USA

9 *Correspondence to:* Ian Baker (ian.baker@dartmouth.edu)

10 **Abstract**

11 To improve our understanding of firn compaction and deformation processes, constant-load
12 compressive creep tests were performed on specimens from a Summit, Greenland (72°35' N,
13 38°25' W) firn core that was extracted in June, 2017. Cylindrical specimens were tested at
14 temperatures of -5°C, -18°C and -30°C from depths of 20 m, 40 m and 60 m at stresses of 0.21
15 MPa, 0.32 MPa and 0.43MPa, respectively. The microstructures were characterized before and
16 after creep using both X-ray micro-computed tomography (micro-CT) and thin sections viewed
17 between optical crossed polarizers. The results of these experiments comprise a novel data set on
18 the creep of firn at three depths of a firn column at three different temperatures, providing useful
19 calibration data for firn model development. Examining the resulting strain vs. time and strain vs.
20 strain rate curves from the creep tests revealed the following notable features. First, the time
21 exponent k was found to be 0.34–0.69 during transient creep, which is greater than the 0.33
22 usually observed in fully-dense ice. Second, the strain rate minimum (SRmin) in secondary creep
23 occurred at a greater strain from specimens with lower density and at higher temperatures. Third,
24 tertiary creep occurred more easily for the lower-density specimens at greater effective stresses
25 and higher temperatures, where strain softening is primarily due to recrystallization. Fourth, the
26 SRmin is a function of the temperature for a given firn density. Lastly, we developed empirical
27 equations for inferring the SRmin, as it is difficult to measure during creep at low temperatures.
28 The creep behaviors of polar firn, being essentially different from full-density ice, imply that firn
29 densification is an indispensable process within the snow-to-ice transition, particularly firn
30 deformation at different temperatures connected to a changing climate.

31

32 **Keywords:** **Firn densification**; Creep; Activation energy; **Cryospheric micro-CT**; Temperature

33 1. Introduction

34 Understanding firn compaction and densification experimentally is critical for developing
35 physics-based firn models that are necessary for many glaciological applications, e.g.
36 reconstructing ice-core paleoclimate records, interpreting ice-mass changes from satellite
37 altimetry data, and even developing clean hydrogen production and storage technology (Li, 2023a;
38 2024a; 2024b; 2024c). However, the firn models used for these applications are empirical and are
39 known to perform poorly outside of their calibration range (Lundin et al., 2017). Thus, a better
40 understanding of firn compaction is necessary to refine firn models for these important
41 glaciological applications. Laboratory compressive experiments on firn and ice improve our
42 understanding of their respective flow laws and advance the development of firn models under a
43 range of conditions. The rheology of polycrystalline ice, particularly its temperature-dependent
44 creep deformation, is a cornerstone of glaciological modeling. Numerous studies have established
45 a robust framework for understanding ice deformation, primarily through laboratory creep
46 experiments (e.g. Glen, 1955; Weertman, 1983; Budd and Jacka, 1989; Durham et al., 2001;
47 Goldsby and Kohlstedt, 2001; Petrenko and Whitworth, 1999). This body of work has confirmed
48 that ice creep is strongly governed by temperature, typically described by an Arrhenius
49 relationship with a well-constrained activation energy for grain-scale processes like dislocation
50 glide and climb (e.g. Jacka, 1984; Hooke, 2005). In contrast, the mechanical behavior of firn, the
51 intermediate porous material between snow and glacial ice, remains comparatively poorly
52 characterized, especially with respect to temperature. It is important to note that “the experimental
53 observations are discussed with respect to the mechanical properties of polycrystalline ice, which
54 is the constituent material of the load-bearing ice skeleton” (Scapozza and Bartelt, 2003), sharing

55 poromechanics-based deformation mechanisms between the two via continuum mechanics and
56 homogenization framework (Gagliardini and Meyssonier, 2000; Coussy, 2004; Hutter and Johnk,
57 2004; Srivastava et al., 2010). While numerous studies have investigated firn and ice deformation
58 (e.g. Steinemann, 1954; Landauer, 1958; Mellor, 1975; Salm, 1982; Maeno and Ebinuma, 1983;
59 Ambach and Eisner, 1985; Li et al., 1996; Meussen et al., 1999; Bartelt and von Moos, 2000;
60 Jacka and Li, 2000; Song et al., 2006a, 2006b, 2008; Theile et al., 2011; Treverrow et al., 2012;
61 Hammonds and Baker, 2016, 2018; Li and Baker, 2021, 2022a), existing firn data are sparse and
62 fragmented. A critical knowledge gap persists in the systematic experimental quantification of
63 firn's mechanical response across a broad range of temperatures. Temperature is a first-order
64 control on firn densification and deformation rates, yet most laboratory studies have been
65 conducted at a limited number of isothermal conditions, often focused on a single density or at
66 temperatures near the melting point (e.g. Mellor, 1975; Maeno and Ebinuma, 1983). Consequently,
67 there is a pronounced lack of experimental data necessary to derive the systematic activation
68 energy for the creep of firn over its full density spectrum. This parameter is not merely a scalar
69 but is likely a function of density, microstructure, and the dominant deformation mechanism
70 (compaction versus shear), transitioning from grain-boundary sliding in low-density firn to
71 dislocation creep in high-density firn and ice (Hammonds and Baker, 2018; Li, 2022; Li and
72 Baker, 2022a). The absence of comprehensive, temperature-variable creep data for firn across its
73 density range renders it insufficient for constraining the temperature-dependence terms in modern,
74 physics-based firn models. Our work fills this gap via X-ray micro-computed
75 tomography-analyzed mechanical examinations, e.g. a systematic series of constant-stress creep
76 experiments on firn cores of varying density, conducted across a thermally controlled range from

77 -30°C to -5°C . This allows for the direct determination whether the apparent activation energy is
78 a function of density, thereby providing the essential experimental foundation needed to improve
79 predictions of firm densification in ice-sheet and glacier models. Notably, the mechanical behavior
80 of two-phase flow coupling the airflow with the ice matrix deformation has not yet been
81 performed experimentally hitherto, even though the role of the microstructures of firm on airflow
82 has been studied (Albert et al., 2000; Courville et al., 2010; Adolph and Albert, 2014). This
83 difficulty is largely due to the limitations of the observation techniques of nondestructive
84 visualization of the microstructures during snow and firm deformation. Thus, caution should be
85 taken when extending the conclusions to ice sheet and glacier scales from sample laboratory
86 experiments. Macroscopically, the creep of firm obeys a power-law dependence of the strain rate
87 on the stress at constant stresses and temperature, similar to that of full-density ice (Li and Baker,
88 2022a). Note that both the diffusivity and permeability of the air in the pores (Albert et al., 2000;
89 Courville et al., 2010; Adolph and Albert, 2014) impact heat conduction of the ice matrix, and
90 hence the grain growth. This is tightly tied to the micro-mechanisms, e.g. grain-boundary and
91 lattice diffusion of the ice crystals (Li and Baker, 2021), superplastic deformation and
92 inter-particle sliding from dislocation motion in the ice necks (Bartelt and Von Moos, 2000), and
93 likely rearrangement of the ice particles (Perutz and Seligman, 1939; Anderson and Benson, 1963;
94 Ebinuma and Maeno, 1987).

95
96 Through experiments on isotropic ice samples subjected to uni-axial compaction at octahedral
97 stresses of 0.1–0.8 MPa and temperatures from -45°C to -5°C , Jacka and Li (2000) determined
98 the mechanisms involved in the empirical *power-law flow*, which was derived by Glen (1955) for

99 stresses ranging from 0.1–1 MPa at temperatures spanning from -13°C to the melting-point. They
100 found that dynamic recrystallization predominated at higher temperatures and stresses, whereas
101 crystal rotation governed at lower temperatures and stresses. Later, Goldsby and Kohstedt (2001)
102 found that ice could exhibit *superplastic flow*, which depends inversely on the grain size,
103 particularly for fine-grained ice, while both dislocation creep and basal slip-limited creep were
104 unrelated to the grain size at stresses of 0.1 MPa or less over a wide range of temperatures.
105 Moreover, Baker and Gerberich (1979) reported that the apparent activation energy for creep for
106 polycrystalline ice, which was derived from tests at constant stress and temperatures ranging from
107 -40°C to -5°C , increased with increasing volume fraction of inclusions (bubbles, impurities, dust,
108 and air clathrate hydrates). Such inclusions governed the evolution of grain size related to thermal
109 activations. The activation energies for the creep of snow and ice have been determined by a
110 number of authors, and values ranging from 58.6–113 kJ mol^{-1} were obtained under both uniaxial
111 and hydrostatic experiments for snow with a density of $\sim 400 \text{ kg m}^{-3}$ at -13.6°C to -3.6°C
112 (Landauer, 1958); 44.8–74.5 kJ mol^{-1} from snow with densities of 440–830 kg m^{-3} at -34.5°C to $-$
113 0.5°C (Mellor and Smith, 1966); $\sim 72.9 \text{ kJ mol}^{-1}$ for firn with a density of 320–650 kg m^{-3} at the
114 South Pole (Gow, 1969); $69 \pm 5 \text{ kJ mol}^{-1}$ for a mean snow density of $423 \pm 8 \text{ kg m}^{-3}$ at -19°C to
115 -11°C (Scapozza and Bartelt, 2003); the 78 kJ mol^{-1} from polycrystalline ice compression
116 deformation at a temperature of -10°C (Duval and Ashby, 1983); $\sim 60 \text{ kJ mol}^{-1}$ for artificial and
117 natural ice at the South Pole (Pimienta and Duval, 1987); and $78 \pm 4 \text{ kJ mol}^{-1}$ for monocrystal ice
118 at -20°C to -4.5°C and $75 \pm 2 \text{ kJ mol}^{-1}$ for bicrystal ice at -15°C to -4.5°C (Homer and Glen,
119 1978). In summary, the flow law of polycrystalline ice and firn depends on the effects of
120 recrystallization, grain size, inclusions (Mellor and Testa, 1969; Vickers and Greenfield, 1968;

121 Barnes et al., 1971; Baker and Gerberich, 1979; Goodman et al., 1981), and the temperature.

122

123 With advanced observation techniques, the relevant microstructural parameters of snow and firn
124 have been characterized by a number of scientists (Arnaud et al., 1998; Coleou et al., 2001; Flin et
125 al., 2004; Wang and Baker, 2013; Wiese and Schneebeli, 2017; Li, 2022). Using X-ray
126 micro-computed tomography (micro-CT), Li and Baker (2022b) characterized metamorphism
127 from snow to depth hoar under opposing temperature gradients. Only rarely has work been
128 performed on the co-effects of temperature and stress on the densification of firn while
129 simultaneously visualizing the microstructural changes using a micro-CT. For example, Schleef et
130 al. (2014) reported that densification under varying conditions of overburden stress and
131 temperature from natural and laboratory-grown new snow showed a linear relationship between
132 density and the specific surface area (SSA). To this end, the aim of our present work is to
133 investigate the temperature dependence of the creep of polar firn and relate this to the change of
134 microstructure determined using micro-CT studies on firn obtained from Summit, Greenland in
135 2017. As is well known, temperature is a key parameter affecting the flow of firn and ice, and
136 plays a determined role in their deformation, especially for polythermal and temperate glaciers.
137 Due to the great difficulty of analyzing firn and ice deformation with the presence of liquid water,
138 this work focuses on the firn creep from the dry snow zone, i.e., areas without meltwater, at
139 different temperatures.

140

141 **2. Samples and measurements**

142 *2.1 Samples*

143 Three cylindrical samples (22 ± 0.5 mm diameter; 50 ± 0.5 mm high) were produced at each of
144 three depths of 20 m, 40 m and 60 m from the same 2017 Summit, Greenland firn core that was
145 studied in Li and Baker (2022a). Both the densities and porosities of these above samples are
146 typical of values in the snow-to-ice transition zone as introduced in Section 1. It is important to
147 note that the reduction in effective stress with increasing depth is evident in samples taken from
148 these three specified depths (**Appendix A**). Before creep testing, one cylindrical firn samples
149 from each depth was stored at a temperature of $-5 \pm 0.5^\circ\text{C}$, $-18 \pm 0.5^\circ\text{C}$, and $-30 \pm 0.5^\circ\text{C}$ for two
150 days to achieve thermal equilibrium (Li and Baker, 2022a). It's also important to note that firn is a
151 heterogeneous material that can have variations in layering, fabric, grain size, and impurity
152 concentration across short distances. Thus, care was taken to extract the three replicate samples
153 from the core at each depth as closely as possible to reduce the variability in their initial
154 conditions.

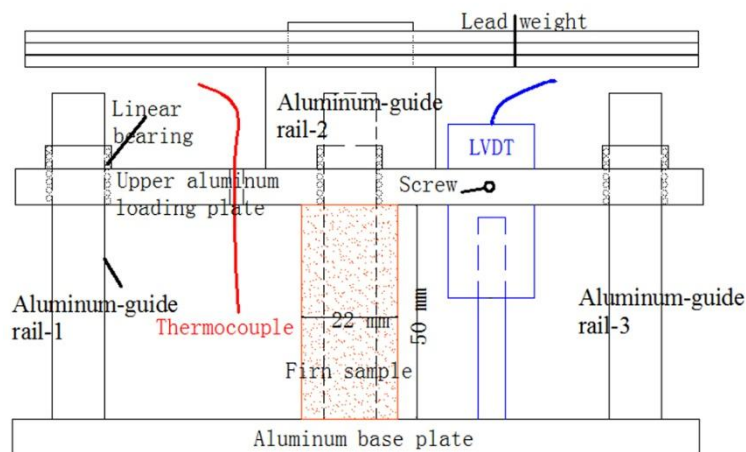
155

156 *2.2 Creep measurements*

157 Three home-built creep jigs were placed in individual Styrofoam boxes in three different cold
158 rooms that were held at temperatures of $-5 \pm 0.5^\circ\text{C}$, $-18 \pm 0.5^\circ\text{C}$ and $-30 \pm 0.5^\circ\text{C}$. Each creep jig
159 consists of an aluminum base plate and three polished aluminum-guide rails passing through
160 linear bearings that hold the upper aluminum loading plate (**Figure 1**). A linear voltage
161 differential transducer (LVDT-Omega LD-320: resolution of 0.025%; linearity error of $\pm 0.15\%$
162 of full-scale output), parallel to the three aluminum-guide rails, was located adjacent to the center
163 of the upper plate, and fixed firmly using a screw through the plate (**Figure 1**) for measuring the
164 displacement during a test. The displacement was logged every 5 seconds using a Grant SQ2010

165 datalogger (accuracy of 0.1%). Temperatures were logged at 300-second time intervals over the
 166 entire test period, using a k-type thermocouple (Omega RDXL4SD thermistor: resolution of 0.1°C)
 167 that was mounted inside each box. In this work, specimens were tested at temperatures of $-5 \pm$
 168 0.2°C , $-18 \pm 0.2^\circ\text{C}$ and $-30 \pm 0.2^\circ\text{C}$ from depths of 20 m (applied stress 0.21 MPa), 40 m (0.32
 169 MPa) and 60 m (0.43 MPa). There are smaller error bars for the temperature of the specimens
 170 than the room temperature because the creep jigs were in insulated Styrofoam boxes. The stresses
 171 were chosen based on experience from previous tests (Li and Baker, 2022a) in order to give
 172 measurable creep rates in a reasonable time.

173



174

175 **Figure 1:** Schematic illustrating the home-built compressive creep jigs. More details can be found
 176 in (Li & Baker, 2022a).

177

178

179 2.3 X-ray micro-computed tomography (micro-CT)

180 Each specimen at each depth and temperature combination was scanned using a Skyscan 1172
 181 micro-CT, before and after creep testing. Each micro-CT scan lasted ~ 2 h. The cubic Volume of

182 Interest (VOI, a side length of 8 mm) was taken from near the center of the firn specimen as
183 conducted in Li and Baker (2022a). The microstructural parameters obtained from the micro-CT
184 data are the SSA, the mean structure thickness of the ice matrix (S.Th), the area-equivalent circle
185 diameter of the pores (ECDA), the total porosity (TP), the closed porosity (CP), and the structure
186 model index (SMI). The SSA (mm^{-1}) is the ratio of the ice surface area to total firn volume (ice
187 plus air) in a VOI analytical element, and is calculated using the hexahedral marching cubes
188 algorithm via CTAn software (Wang and Baker, 2013). It characterizes the thickness and
189 complexity of the firn microstructure. Changes in SSA indicate a change in free energy of the ice
190 surfaces, the decrease of which represents the occurrence of sintering-pressure. The S.Th (mm) is
191 the mean structure thickness of an ice matrix (Hildebrand and Ruesegger, 1997), which
192 represents the characteristic size of an ice particle in the firn, where the ice particle consists of one
193 or many crystals or grains. It is measured based on the largest sphere diameter that encloses a
194 point in the ice matrix and is completely bounded within solid surfaces. The ECDA (mm) is the
195 diameter of a circle having the same area as the average for all pores in the VOI from the 2-D
196 binary images, indicative of the characteristic size for the void space (Adolph and Albert, 2014).
197 The TP (%) is the ratio of the pore volume, including both open and closed pores, to the total VOI.
198 The CP (%) is the ratio of the volume of the closed pores to the total volume of solid plus closed
199 pores volume in a VOI, while the open porosity (%) is the ratio of the volume of the open pores to
200 the total VOI. The SMI is calculated based on the dilation of a 3-D voxel model (Hildebrand and
201 Ruesegger, 1997) $SMI = 6(S' \times V) / S^2$, where S' is the change in the surface area due to
202 dilation, and V and S are the object volume and surface area, respectively. It indicates the
203 prevalent ice curvature, negative values of which represent a concave surface, e.g. the hollow air

204 structure surrounded by an ice matrix. The more negative the SMI value, the more spherical the
205 pore. Notably, the micro-CT-derived density of each specimen agrees well with the bulk density
206 measured using the mass-volume approach (Li and Baker, 2021).

207

208 *2.4 Thin section preparation and imaging*

209 Thin sections for optical photographs before and after creep testing were cut from bulk specimens,
210 one side of which was first smoothed with a microtome. This side was then frozen onto a glass
211 plate ($100 \times 60 \times 2$ mm) by dropping supercooled gas-free water along its edges. Its thickness
212 was reduced to ~ 2 mm by a band saw, and finally thinned further to a uniform thickness of ~ 0.5
213 mm using a microtome. Images were captured using a digital camera after each thin section was
214 placed on a light table between a pair of crossed polarizing sheets.

215

216 **3 Results and discussion**

217 *3.1 Microstructures before creep*

218 Increasing firn density with increasing depth from either of the -5°C , -18°C , and -30°C
219 specimens can be readily recognized by visual inspection of the micro-CT 3-D reconstructions of
220 the firn microstructure (**Figure 2**). Correspondingly, the microstructural parameters, with the
221 exception of the CP, changed monotonically with increasing depth at each temperature, e.g. the $-$
222 30°C samples increased in density from $591 \pm 1.4 \text{ kg m}^{-3}$, to $683 \pm 4.2 \text{ kg m}^{-3}$, to $782 \pm 1.5 \text{ kg m}^{-3}$,
223 decreased in SSA from $4.64 \pm 0.04 \text{ mm}^{-1}$, to $3.3 \pm 0.06 \text{ mm}^{-1}$, to $2.39 \pm 0.01 \text{ mm}^{-1}$, and decreased
224 in TP from $35.6 \pm 0.05\%$, $25.6 \pm 0.4\%$, to $14.8 \pm 0.2\%$ at 20, 40, and 60 m, respectively (**Table 1**).

225 These above changes are similar to those previously observed in this firn core (Li and Baker,

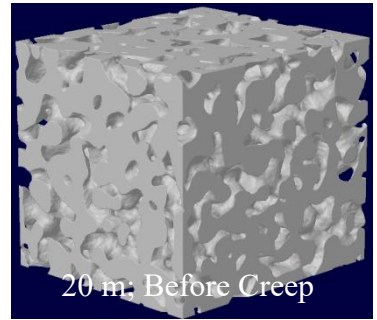
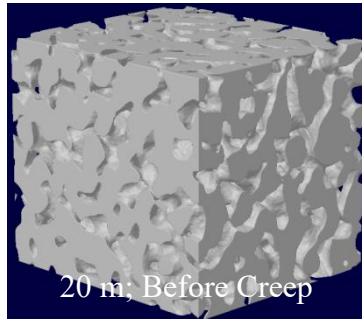
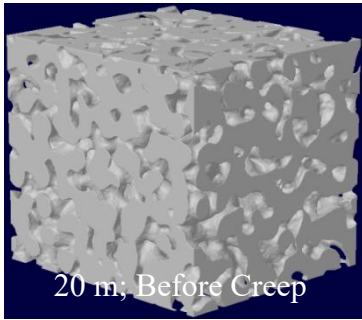
226 2022a), implying that the sintering-pressure mechanism plays a crucial role in the densification of
227 polar firn due to the increasing overburden of snow and firn with increasing depth. However, the
228 microstructures of the samples from the three temperatures at each depth show little variability
229 and do not monotonically change with temperature, e.g. at 20 m depth the -5°C , -18°C , and $-$
230 30°C samples having densities of $589 \pm 1.3 \text{ kg m}^{-3}$, $615 \pm 2.5 \text{ kg m}^{-3}$, and $591 \pm 1.4 \text{ kg m}^{-3}$, and

231

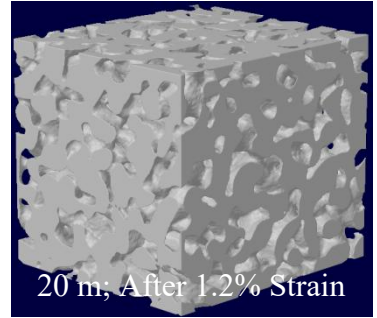
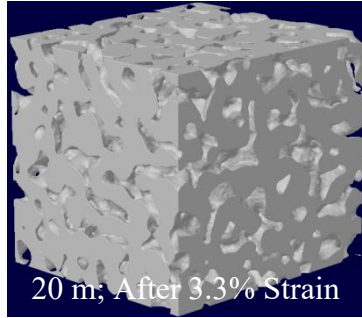
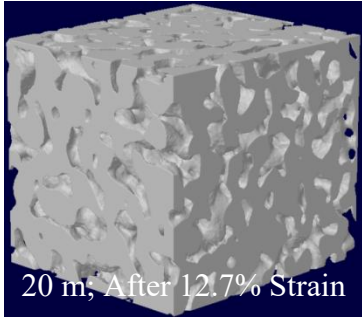
-5°C

-18°C

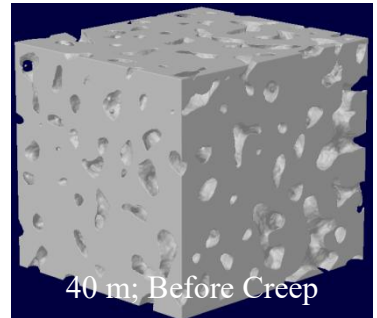
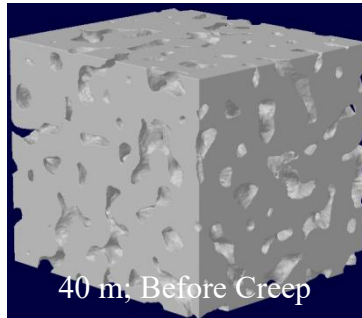
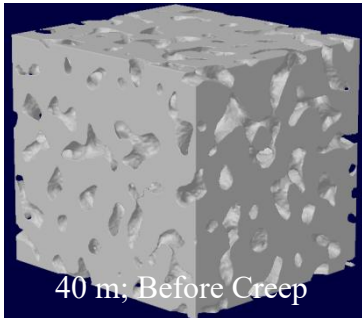
-30°C



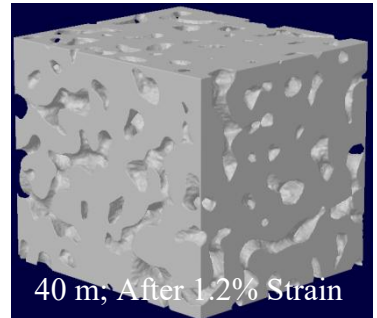
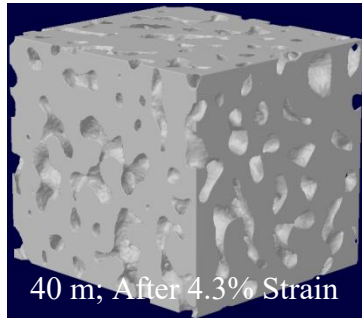
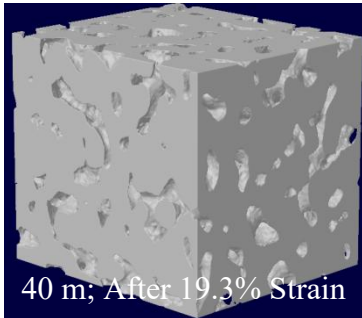
232



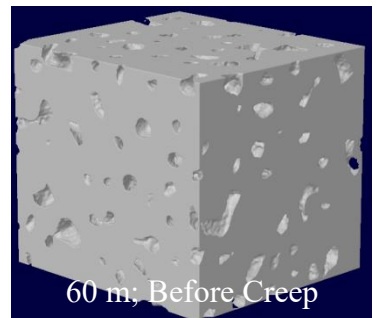
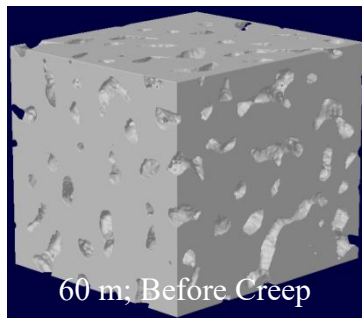
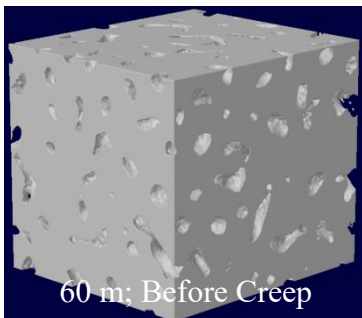
233



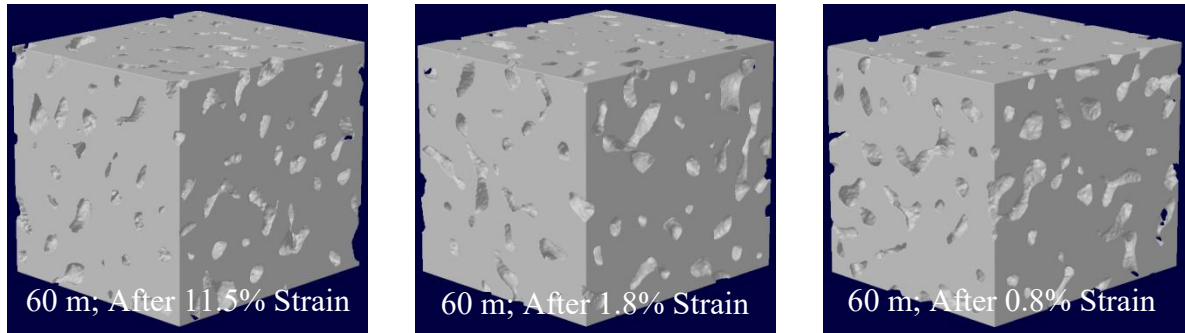
234



235



236



237

238 **Figure 2:** Micro-CT 3-D reconstructions (the side length of each cubic volume of interest is 8 mm)

239 of specimens before and after creep testing at the depths and temperatures shown. Grey voxels
 240 represent ice in the firm structure.

241

242

243 Table 1. Microstructural parameters derived from Micro-CT for samples at -5°C , -18°C , and $-$
 244 30°C from depths of 20 m, 40 m, and 60 m before creep.

20m							
T $^{\circ}\text{C}$	Density kg m^{-3}	SSA mm^{-1}	S.Th mm	TP %	CP %	SMI	ECDa mm
-5	589±1.3	4.74±0.03	0.732±0.001	35.9±0.08	0.03±0.002	-0.31±0.04	1.07±0.005
-18	615±2.5	4.51±0.04	0.758±0.001	33.1±0.2	0.01±0.001	-0.57±0.01	0.995±0.013
-30	591±1.4	4.64±0.04	0.747±0.004	35.6±0.05	0.02±0.001	-0.27±0.05	1.09±0.004
40m							
T $^{\circ}\text{C}$	Density kg m^{-3}	SSA mm^{-1}	S.Th mm	TP %	CP %	SMI	ECDa mm
-5	685±1.4	3.26±0.04	0.95±0.004	25.5±0.1	0.015±0.001	-1.85±0.11	0.857 ±0.005
-18	669±0.6	3.41±0.04	0.914±0.003	27.1±0.03	0.01±0.001	-1.69±0.09	0.892±0.002
-30	683±4.2	3.30±0.06	0.94±0.01	25.6±0.4	0.021±0.005	-1.87±0.13	0.86±0.01
60m							
T $^{\circ}\text{C}$	Density kg m^{-3}	SSA mm^{-1}	S.Th mm	TP %	CP %	SMI	ECDa mm
-5	790±1.0	2.34±0.03	1.1±0.003	14.0±0.1	0.11±0.01	-4.81±0.22	0.594±0.003
-18	780±0.5	2.37±0.03	1.08±0.01	15.2±0.06	0.014±0.007	-4.8±0.2	0.632±0.001
-30	782±1.5	2.39±0.01	1.076±0.0003	14.8±0.2	0.02±0.001	-4.92±0.14	0.639±0.002

247 Note: SSA is the specific surface area, S.Th is the structure thickness, TP is the total porosity, CP

248 is the closed porosity, SMI is the structure model index, and ECDA is the area-equivalent circle
249 diameter.

250

251

252 SSAs of $4.74 \pm 0.03 \text{ mm}^{-1}$, $4.51 \pm 0.04 \text{ mm}^{-1}$, and $4.64 \pm 0.04 \text{ mm}^{-1}$, respectively (**Figures 2–3;**
253 **Table 1**). Here, despite the -18°C specimen having a higher density than the two others at -5°C
254 and -30°C , is not possible to conclude that the sintering of firm is not directly related to the
255 temperature. This is likely because a thermal equilibration period of two days in the absence of
256 compression is too short to sufficiently exert the influence of temperature on firm sintering. The
257 microstructural differences seen in these specimens more likely arose from the initial samples
258 themselves, which were anisotropic and heterogeneous even if taken from the same depth,
259 attributed to firm pre-deformation and partial annealing before experiments (Li and Baker, 2022a).

260

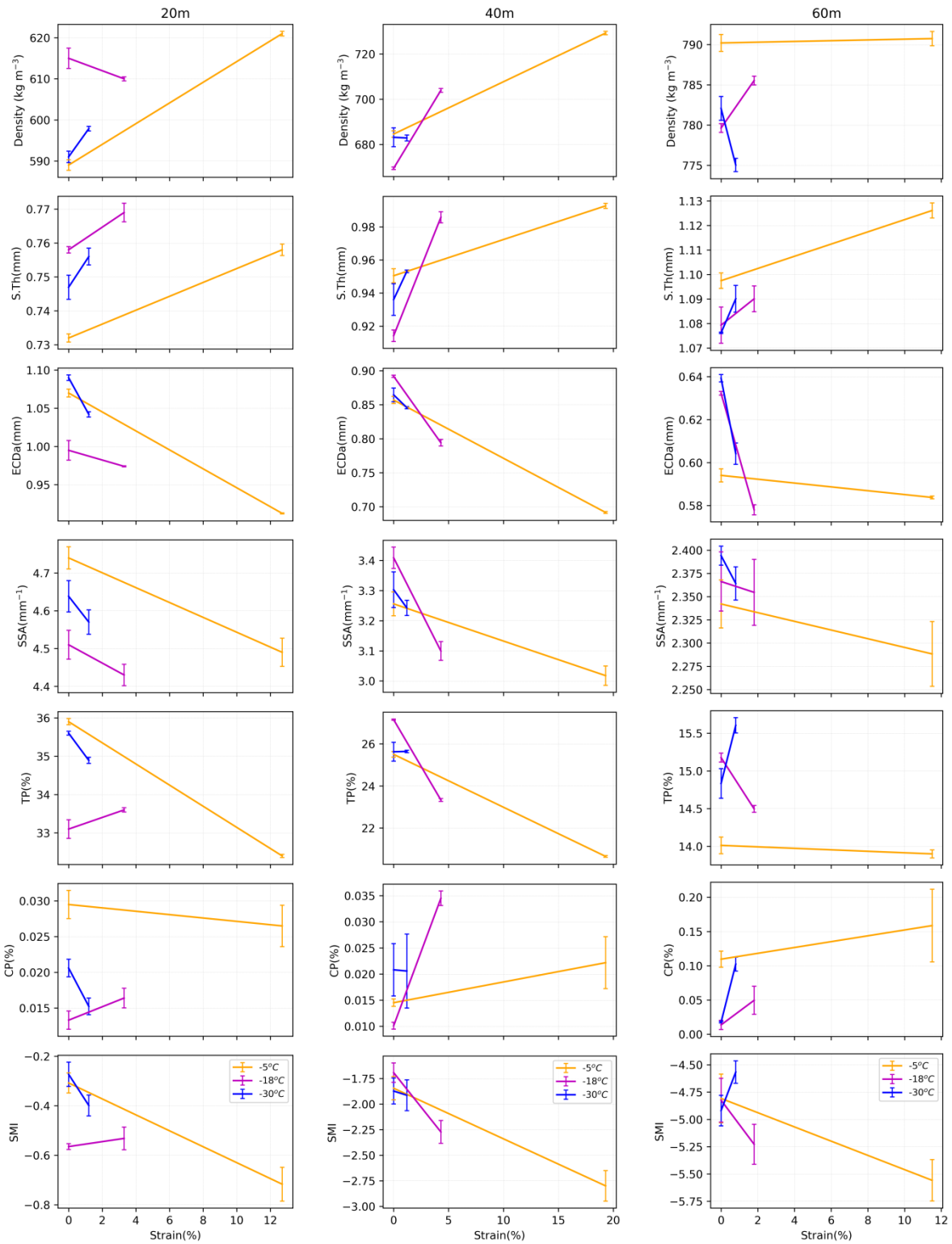
261 3.2 Microstructures after creep

262 The microstructural evolution is characterized by the microstructural parameters shown in **Figure**
263 **3**. The largest changes occurred in the -5°C specimens due to the higher temperature, i.e., the
264 density, S.Th, and CP increased, while the ECDA, TP, SSA, and SMI decreased, indicative of
265 consolidation of the firm after creep. It is important to note that for the 60 m sample tested at -5°C ,
266 there was no change in density, i.e., $790.2 \pm 1 \text{ kg m}^{-3}$ before creep vs. $790.7 \pm 0.9 \text{ kg m}^{-3}$ after
267 creep, or TP, i.e., $14.0 \pm 0.1\%$ before creep vs. $13.9 \pm 0.1\%$ after creep. This lack of
268 microstructural change is due to the high initial density, which was close to the firm pore close-off
269 density of $\sim 830 \text{ kg m}^{-3}$. Thus, the creep of this sample may involve a transition from firm to

270 bubbly ice, as is also indicated by the increase in CP, which would have made it difficult to
271 compress further. Intriguingly, some of the changes in microstructure observed in the micro-CT
272 3-D reconstructions from the specimens before and after creep, e.g. the distribution of ice-space,
273 are indistinguishable in **Figure 2**. This is presumably due to the relatively large initial particle size,
274 or from radial dilation exceeding the axial compression because of the small strains that occurred
275 at relatively low temperatures.

276

277 One exception to the expected microstructural change after creep was the decrease of CP, which
278 was likely due to the measurement uncertainty of the micro-CT (Burr et al., 2018), or radial
279 expansion of the specimen during creep. Another exception was the decrease in density after
280 creep for the -18°C specimen at 20 m and the -30°C specimen at 60 m, which arose due to a
281 de-densification effect produced by temperature gradient metamorphism, as confirmed by the
282 increase of both TP and S.Th (Li and Baker, 2022b). The thermal gradient appears to be
283 associated with a fluctuation of 0.2°C around the test temperature, similar to temperature cycling
284 occurred within firn (Mellor and Testa, 1969; Weertman, 1985), which stems from the
285 thermometer's inherent accuracy as noted in Section 2.2 ($-5 \pm 0.2^{\circ}\text{C}$, $-18 \pm 0.2^{\circ}\text{C}$ and $-30 \pm$
286 0.2°C). In the relatively simple deformation found at ice-sheet dome sites, such as Summit, there
287 is no mechanism to decrease density during compression. At sites closer to the ice sheet margins,
288 cracking due to extension of the ice may cause a localized decrease in density. The rate of firn
289 densification should decrease with increasing depth at a given temperature, due to the decrease of
290 effective stress with increasing depth (**Appendix A**). As a matter of fact, the density of the -5°C
291 samples after creep increased by 32 kg m^{-3} , 44 kg m^{-3} , and 0.5 kg m^{-3} for the 20 m, 40



292

293 **Figure 3:** Density, structure thickness (S.Th), area-equivalent circle diameter (ECDA), specific
 294 surface area (SSA), total porosity (TP), closed porosity (CP), and structure model index (SMI) of
 295 the firm samples before and after creep at three temperatures (orange, magenta, and blue lines)

296 from depths of 20 m, 40 m and 60 m. Error bars indicate the variation of each microstructural
297 parameter as derived from three different VOIs of the same sample.

298

299

300 m, and 60 m samples, respectively. The 44 kg m⁻³ unexpectedly outnumbers the 32 kg m⁻³,
301 implying that the densification of firn is also affected by other undetermined factors, e.g. the
302 effect of inclusions, in addition to the stress and temperature.

303

304 Another way to investigate microstructure changes before and after creep tests is to compare their
305 grain sizes using thin sections. As an example, **Figure 4** shows optical micrographs of thin
306 sections made from the -5°C sample at 40 m before and after creep to a strain of 19.3%, where
307 the significant reduction in grain size from 0.8 ± 0.67 mm to 0.5 ± 0.32 mm implies the
308 occurrence of recrystallization during testing. However, it is also unclear at what strain
309 recrystallization

310

311

312

313

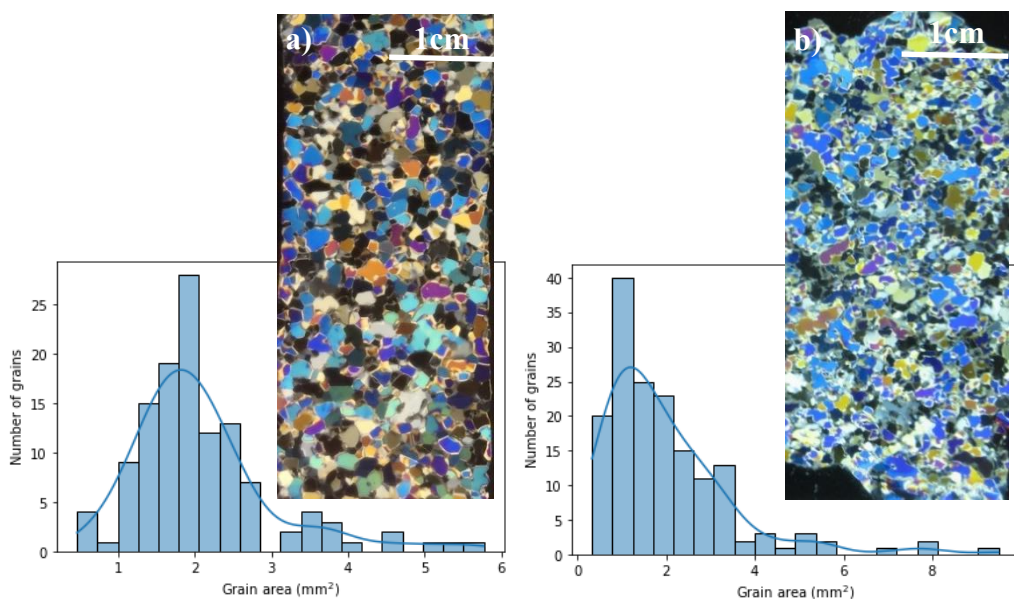
314

315

316

317

318



319 **Figure 4:** Optical micrographs of thin sections, and the distribution of grain sizes for the 40 m sample
320 at -5°C (a) before and (b) after creep (19.3% strain).

321

322

323 was initiated in each test, as noted in Li and Baker (2022a). Recrystallization occurs frequently at
324 a temperature higher than the homologous temperatures of $0.9 T_m$. However, no evidence was
325 found for recrystallization after testing at the relatively cold -18°C and -30°C conditions,
326 probably due to the small creep strains at these relatively low temperatures. The creep
327 mechanisms for these samples, and whether the mechanisms were different at different
328 temperatures, could not be determined from the micro-CT-derived microstructural observations
329 alone, because the micro-CT can only capture the microstructure before and after creep. Instead,
330 plots of both strain vs. time and strain rate vs. strain can be used to elucidate the onset of
331 recrystallization during creep (Sections 3.3 and 3.4; Ogunmolasuyi, et al., 2023).

332

333 *3.3 Relationship between strain and time*

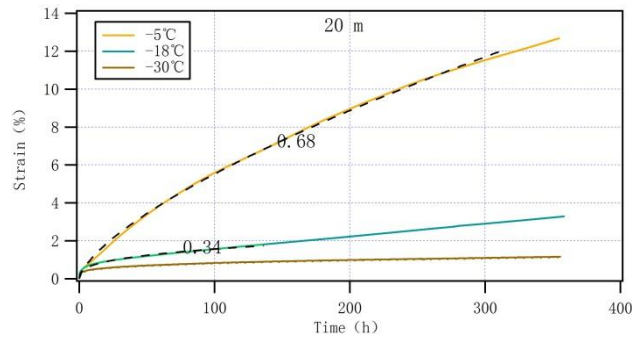
334 **Figure 5** shows the strain vs. time creep curves. The specimens at -5°C at 20 m and -18°C at 20
335 m, 40 m, and 60 m, show decelerating transient creep and quasi-viscous steady-state creep, while
336 the specimens at -5°C at 40 m and 60 m show transient, secondary, and accelerating tertiary creep.
337 Note that the curves from the -30°C specimens are not easily interpreted due to a large amount of
338 noise arising from both the insufficient resolution of a linear voltage differential transducer (Li
339 and Baker, 2022a) and the very small strains. The transient creep stage may be caused by strain
340 hardening that occurs from the yield point to the ultimate strength (Glen, 1955; Jacka, 1984). The

341 plastic deformation is accommodated by an increase in dislocation density through dislocation
342 multiplication or the formation of new dislocations (Frost and Ashby, 1982; Duval et al., 1983;
343 Ashby and Duval, 1985), which leads to an increase of the firm strength as the dislocations
344 become pinned or tangled, and thus more difficult to move. The initial decrease of creep rate may
345 also be related to the rearrangement of dislocations into a more stable pattern through a dragging
346 mechanism (Weertman, 1983) for the -5°C specimens. The tertiary creep stage may be associated
347 with strain softening deriving either from the thermally-activated processes at the high
348 homologous temperature approaching the melting point of ice, or from recrystallization (Li and
349 Baker, 2022a). Clearly, the creep rate of firm is sensitive to temperature under constant stress at a
350 given depth, *viz.*, the creep rate increases with increasing temperature (**Figure 5**). Incidentally,
351 there is no evidence of the onset of recrystallization in the creep curves themselves despite the
352 thin-section observation that -5°C specimens clearly underwent recrystallization during creep
353 (Section 3.2).

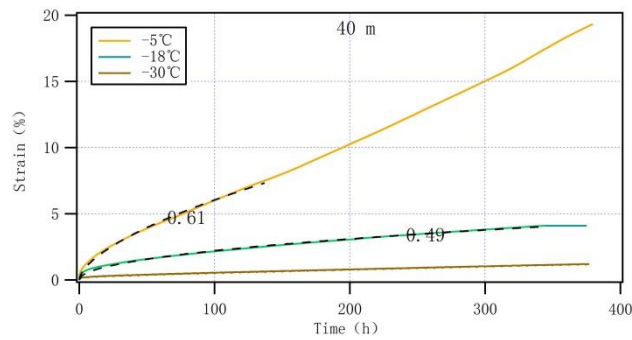
354

355 A modified Andrade-like equation $\varepsilon = \beta t^k + \varepsilon_0$ in Li and Baker (2022a) was used to describe the
356 transient creep behavior of the firm, in which the primary creep was well represented in black
357 dashed lines on the creep curves in **Figure 5**. The time exponent k , derived from the above
358 equation, ranges from 0.34–0.69: the data for the -30°C specimens are excluded since the noise in
359 the results makes them uninterpretable. These k values are also smaller than those from
360 monocrystalline and bicrystalline ice: 1.9 ± 0.5 , 1.5 ± 0.2 , and 1.3 ± 0.4 (Li and Baker, 2022a and
361 references therein). We also note that the k values from the specimens at -5°C from 20–60 m

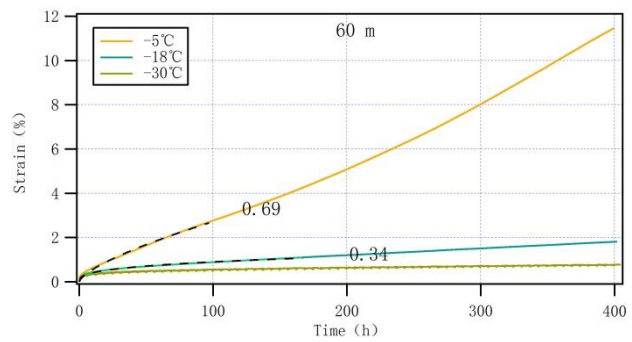
362



363



364



365

366 **Figure 5:** Strain vs. time for firm specimens at -5°C (yellow lines), -18°C (blue lines), and -30°C
367 (brown lines), from depths of 20 m (applied stress 0.21 MPa), 40 m (0.32MPa) and 60 m
368 (0.43MPa). The black dashed curves represent fits to a modified Andrade-like equation with the
369 time exponents indicated on the curves, if any.

370

371

372 (0.68, 0.61, and 0.69), and at -18°C from 40 m (0.49) are greater than 0.33, while the k value
373 from the -18°C specimens at 20 m (0.34) and 60 m (0.34) are close to 0.33 that is usually

374 obtained for full-density polycrystal ice. Interestingly, an evident relationship between the density
375 of firm and the k values, regardless of the effect of stress (Li and Baker, 2022a) and temperature,
376 remains unknown. A greater k value signifies faster deformation. The k values derived for firm are
377 generally higher than those for polycrystalline ice, implying that the higher firm deformation rates
378 compared to those of ice are likely related to the fewer grain-boundary constraints with more void
379 space in firm (Li and Baker, 2022a; Li, 2023b). Clearly, the above k values, which increased with
380 increasing temperature (**Figure 5**), indicate that deformation is easier because of the lower
381 viscosity at the higher temperature. Thus, k seems to be a state variable with respect to
382 temperature. In addition, k values greater than 0.33 may be related to the decrease of viscosity of
383 the firm specimens (Freitag et al., 2002; Fujita et al., 2014). k values lower than 0.33 observed
384 under constant load and temperature occurred at relatively low effective stresses (Li and Baker,
385 2022a). However, the steady decrease of k values from -5°C to -18°C remains further
386 investigation. Alternatively, the enhanced cohesion strength in the firm, which resulted from both
387 the ice matrix with higher purity and the stronger bond connection of inter-grains, increases the
388 viscosity of test samples and lowers the k value to less than 0.33.

389

390 3.4 Relationship of strain rate to strain

391 **Figure 6** shows log strain rate vs. strain plots from all the -5°C and -18°C specimens; the -30°C
392 samples are excluded due to noise. The evolution of the strain rate is characterized more clearly in
393 **Figure 6** than in **Figure 5**. Clearly, the strain rate is also a state variable of temperature, where the
394 strain rate increases with increasing temperature for a given strain at a given depth (**Figure 6**;
395 **Table 2**). The strain rate minimum at the secondary creep stage (SRmin) and the strain at the

396

397

398 Table 2. Observed and inferred strain rate minima and strains observed at the strain rate minima.

20 m	SRmin s ⁻¹	PC1-SRmin s ⁻¹	PC2-SRmin s ⁻¹	PC3-SRmin s ⁻¹	Strain %
-5°C	5.53×10 ⁻⁶	5.53×10⁻⁶	1.68×10 ⁻⁶	2.56×10 ⁻⁷	11.8
-18°C	1.36×10 ⁻⁶	1.36×10⁻⁶	2.29×10 ⁻⁷	2.45×10 ⁻⁸	1.81–2.9
-30°C(U)	–	7.14×10 ⁻⁷	2.17×10 ⁻⁷	3.3×10 ⁻⁸	–
-30°C(L)	–	3.16×10 ⁻⁸	9.6×10 ⁻⁹	1.46×10 ⁻⁹	–

399

40 m	SRmin s ⁻¹	PC1-SRmin s ⁻¹	PC2-SRmin s ⁻¹	PC3-SRmin s ⁻¹	Strain %
-5°C	1.03×10 ⁻⁵	3.39×10 ⁻⁵	1.03×10⁻⁵	1.57×10 ⁻⁶	7.5
-18°C	1.4×10 ⁻⁶	8.32×10 ⁻⁶	1.40×10⁻⁶	1.5×10 ⁻⁷	4.1
-30°C(U)	–	4.37×10 ⁻⁶	1.33×10 ⁻⁶	2.03×10 ⁻⁷	–
-30°C(L)	–	1.94×10 ⁻⁷	5.88×10 ⁻⁸	8.97×10 ⁻⁹	–

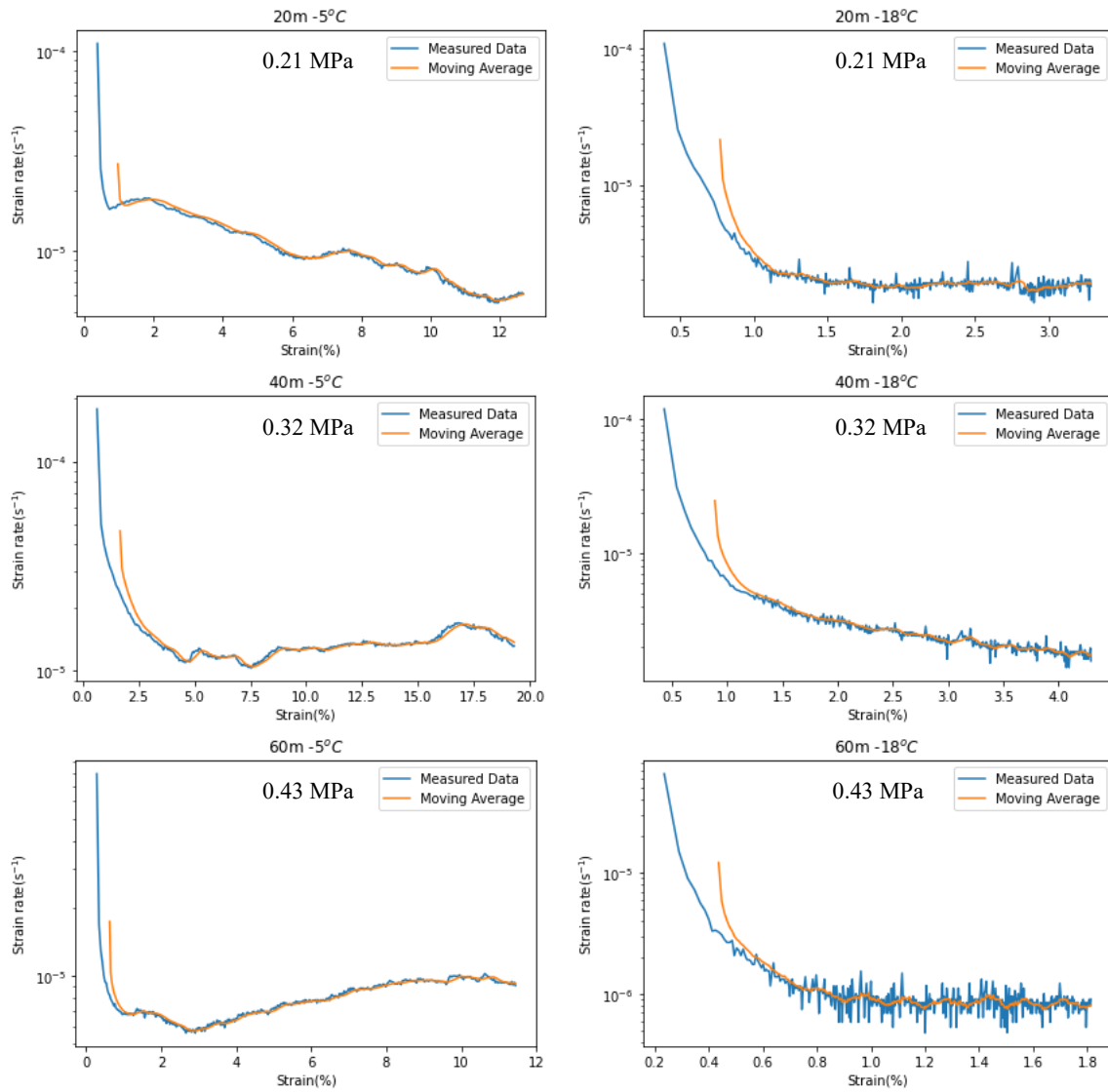
400

60 m	SRmin s ⁻¹	PC1-SRmin s ⁻¹	PC2-SRmin s ⁻¹	PC3-SRmin s ⁻¹	Strain %
-5°C	5.59×10 ⁻⁶	1.21×10 ⁻⁴	3.67×10 ⁻⁵	5.59×10⁻⁶	2.7
-18°C	5.33×10 ⁻⁷	2.96×10 ⁻⁵	4.99×10 ⁻⁶	5.33×10⁻⁷	1.1–1.8
-30°C(U)	–	1.56×10 ⁻⁵	4.74×10 ⁻⁶	7.21×10 ⁻⁷	–
-30°C(L)	–	6.91×10 ⁻⁷	2.1×10 ⁻⁷	3.19×10 ⁻⁸	–

401 The SRmin without the prefix is the observed values during creep, while the SRmin with a prefix
402 is the inferred values. Note that PC-SRmin is the abbreviation of the post-calibration SRmin, and
403 that -30°C(U) and -30°C(L) indicate the upper and lower bound from the -30°C samples from
404 44.8 kJ mol⁻¹ and 113 kJ mol⁻¹, respectively. PC1-SRmin, PC2-SRmin, and PC3-SRmin are
405 described in **Appendix B**. The symbol – indicates the unavailable values of SRmin and the strain
406 value at the SRmin observed during creep. For the italics highlighted, see **Appendix B**.

407

408



409

410

411

412 **Figure 6:** Log strain rate vs. strain from the firm specimens at temperatures of -5°C
 413 from depths of 20 m (applied stress 0.21 MPa), 40 m (0.32MPa) and 60 m (0.43MPa). Samples
 414 from -30°C are not shown due to the very large noise. The blue lines represent discrete strain rates,
 415 which are calculated by extracting the strain data hourly, while the orange lines represent a
 416 moving average of 15 moving windows with respect to the strain.

417

418

419 SRmin for all the -5°C and -18°C specimens are shown in **Figure 6** and **Table 2**. The SRmin was
 420 reached at a strain of 11.8%, 7.5% and 2.7% for the -5°C specimens from depths of 20 m, 40 m,

421 and 60 m, respectively, consistent with strains at the SRmin decreasing with increasing depth at a
422 given temperature in **Figure 8** and **Table 4** in Li and Baker (2022a). For the -18°C specimens,
423 the SRmin occurred over a range of strains from 1.81–2.9% at 20 m, at a fixed strain of 4.1% at
424 40 m, and at a strain oscillating between 1.1 and 1.8% at 60 m. These values of strain at different
425 SRmin values are different from those usually observed at strains of 0.5–3% for fully-dense ice
426 (Cuffey and Paterson, 2010, and references therein), implying different mechanical behavior
427 between firm and pure ice (Duval, 1981; Mellor and Cole, 1983; Jacka, 1984; Li et al., 1996;
428 Jacka and Li, 2000; Song et al., 2005, 2008; Cuffey and Paterson, 2010). Overall, the strain at the
429 SRmin is greater with lower density and higher temperature, e.g. 11.8% strain from the -5°C
430 specimens at 20 m, and 4.1% strain from the -18°C specimens at 40 m. This is likely due to the
431 effect of strain hardening on density and temperature (Li, 2023b). Additionally, tertiary creep is
432 observed during both quasi-steady state deformation, particularly in the -5°C specimens at depths
433 of 40 m and 60 m, and in the ascending stage, as seen in the -5°C and -18°C specimens at 20 m,
434 along with the -18°C specimen at 40 m. This mechanical behavior is facilitated by lower firm
435 density, increased effective stress, and elevated creep temperatures. For instance, in the -5°C
436 specimens at 20 m, strain softening primarily results from recrystallization (Duval, 1981; Jacka,
437 1984; Jacka and Li, 2000; Song et al., 2005; Faria et al., 2014). Also, the activation of easy slip
438 systems contributes to this process (Jonas and Muller, 1969; Duval and Montagnat, 2002; Alley et
439 al., 2005; Horhold et al., 2012; Fujita et al., 2014; Eichler et al., 2017). It is noteworthy that Jacka
440 and Li (1994) observed that steady-state tertiary ice creep, which is marked by stable grain size, is
441 influenced more by applied stresses than by temperature. This finding suggests that there exists a
442 balance between the activation energies required for grain growth and subdivision at a specific

443 temperature.

444

445 3.5 Apparent activation energy for creep

446 Experimental observations of the SRmin are limited, as they only occurred for the -5°C and at $-$
447 18°C specimens at each depth (**Table 2**). It is hard to achieve the SRmin for all firm specimens in
448 laboratory environments (Landauer, 1958), especially under low temperatures and stresses such as
449 those from the -30°C specimens in this work. To this end, we offer the various possibilities of the
450 SRmin using the evidence we have. The value of the apparent activation energy of creep, Q_c (kJ
451 mol^{-1}), is equal to the slope of a line fitted $\ln \dot{\epsilon}$ versus $1/T$ as did in Goldsby & Kohlstedt (1997;
452 2001), using the Arrhenius relation $\dot{\epsilon} = B\sigma^n \exp(-\frac{Q_c}{RT})$, where $\dot{\epsilon}$ (s^{-1}) is the strain rate, B (s^{-1}
453 Pa^{-n}) is the material parameter, σ (MPa) is the applied stress, n is the creep (stress) exponent, R
454 ($8.314 \text{ J mol}^{-1} \text{ K}^{-1}$) is the gas constant, and T (K) is Kelvin temperature. First, the estimation of
455 Q_c is based on *only* two SRmin values from the -5°C and -18°C samples at each depth (**Table 2**).
456 **Glen-King's model** $\dot{\epsilon} = A \exp(-Q_c/RT) = B\sigma^n \exp(-Q_c/RT)$ treats the pre-factor A , material
457 parameter B , and stress exponent n as constants (Glen, 1955; Goldsby and Kohlstedt, 2001). This
458 simplification is valid by using the unifying concept of normalized effective stress. The effective
459 stress captures the complex multi-physical behavior of the two-phase ice-air system, accounting
460 for: 1) The incompressibility of individual ice grains versus the compressibility of the porous ice
461 skeleton, 2) The coupled flow of ice and air; and 3) The interplay between different strain
462 components (axial, radial, volumetric, and true). This framework is grounded in the principles of
463 poromechanics, originally developed for soils and later applied to snow and ice (Gubler, 1978;
464 Hansen and Brown, 1988; Mahajan and Brown, 1993; Chen and Chen, 1997; Lade and deBoer,

465 1997; Ehlers, 2002; Khalili et al., 2004; Gray and Schrefler, 2007; daSilva et al., 2008; Nuth and
 466 Laloui, 2008). The variability in density for the samples from 20-m depth on the mechanical
 467 behavior are negligible due to a small difference (up to ~4%), between samples, which falls
 468 within an acceptable error range in previous studies. This is likely related to multiple factors,
 469 including the intrinsic properties of the samples, e.g. inclusions (impurities, dust, bubbles,
 470 clathrate hydrates), the effects of deformation and partial annealing of firm due to stress
 471 distribution and temperature changes during drilling, extraction, transportation, or storage, and the
 472 fact that the samples are taken from adjacent parts of the core, and might capture heterogeneous
 473 density layers, as well as potential measurement errors associated with the equipment used. The
 474 Q_c values from the 20 m, 40 m, and 60 m specimens were calculated to be 61.4 kJ mol⁻¹, 87.3 kJ
 475 mol⁻¹, and 102.8 kJ mol⁻¹, respectively (**Figure 7**). Based on the three SRmin from the -5°C and -
 476 18°C samples at 60 m in this work, and from -10°C samples at 60 m in Li and Baker (2022a), a
 477 Q_c value for the 60 m specimen was calculated to be 100.7 kJ mol⁻¹. To see whether or not these
 478 above Q_c values are reliable, we estimated the activation energy of grain-boundary
 479 diffusion/viscosity, Q_{gbd} (kJ mol⁻¹), using the relation $K = (D_t^2 - D_0^2)/t = k \exp(-Q_{\text{gbd}}/RT)$,
 480 in an alternative form of $Q_{\text{gbd}} = -R[\partial \ln K / \partial (1/T)]$, where K is the observed rate of grain
 481 growth (mm² a⁻¹), D_0^2 and D_t^2 are the measured mean grain area (mm²) in a firm sample at the
 482 onset of the creep ($t = 0$), and at the end time of the creep (t -year), and k is a constant grain
 483 growth factor. The grain growth rates are plotted on a logarithmic scale against the reciprocal of T
 484 (**Figure 7**). For changes in grain size from the related specimens before and after creep see **Table**
 485 **3**. Correspondingly, the Q_{gbd} values calculated were 41.4 kJ mol⁻¹, 40.8 kJ mol⁻¹, and 40.9 kJ
 486 mol⁻¹ for the specimens at 20 m, 40 m, and 60 m, respectively. These Q_{gbd} values are comparable

487 to the values of 40.6 kJ mol⁻¹ obtained in laboratory experiments on polycrystalline ice (Jumawan,
488 1972), and 42.4 kJ mol⁻¹ from 13 polar firn cores (Cuffey and Paterson, 2010) for grain-boundary
489 self-diffusion of polycrystalline ice. Further, the ratio of $Q_{\text{gbd}}/Q_{\text{c}}$ is 0.67, 0.47, and 0.4 for the 20 m,
490 40 m, and 60 m specimens, respectively. We noted that the ratio of 0.67 for $Q_{\text{gbd}}/Q_{\text{c}}$ was
491 recommended by Hobbs (1974) and Cuffey and Paterson (2010). The Q_{c} values calculated using
492 the Arrhenius relation for the 40 m and 60 m specimens are likely greater than the actual values,
493 and hence are seemingly less reliable. There is little difference between the two-SRmin-derived
494 Q_{c} value (102.8 kJ mol⁻¹) and the three-SRmin-derived Q_{c} value (100.7 kJ mol⁻¹), implying
495 that these two avenues for calculating Q_{c} have equal utility. Moreover, the above Q_{gbd} values
496 are lower than the 48.6 kJ mol⁻¹ that was inferred by the grain growth rate for firn samples with
497 densities ranging from 320–650 kg m⁻³ from cores drilled at the South Pole, Antarctic (Gow,
498 1969), which makes a ratio of 0.67 for $Q_{\text{gbd}}/Q_{\text{c}}$ an unreliable sole-criterion. In short, it is difficult
499 to assess the reliability of both Q_{c} and Q_{gbd} , as discussed above due to their scatter and debates
500 in the current literature. Thus, these Q_{c} values estimated in this work, ranging from 61.4–102.8
501 kJ mol⁻¹, are reasonable, aligning with the literature range of 44.8–113 kJ mol⁻¹ (**Table 4**).

502

503

504 Table 3. Grain area (mm²) measured from optical thin sections for samples at -5°C, -18°C, and -
505 30°C from depths of 20 m, 40 m, and 60 m before and after creep.

Depth	20 m		40 m		60 m	
T/°C	Before	After	Before	After	Before	After
-5	0.29±0.25	0.42±0.28	0.53±0.32	0.79±0.67	0.78±0.67	0.97±0.8
-18	0.29±0.25	0.34±0.2	0.53±0.32	0.7±0.42	0.78±0.67	0.9±0.59
-30	0.29±0.25	0.31±0.17	0.53±0.32	0.57±0.34	0.78±0.67	0.81±0.56

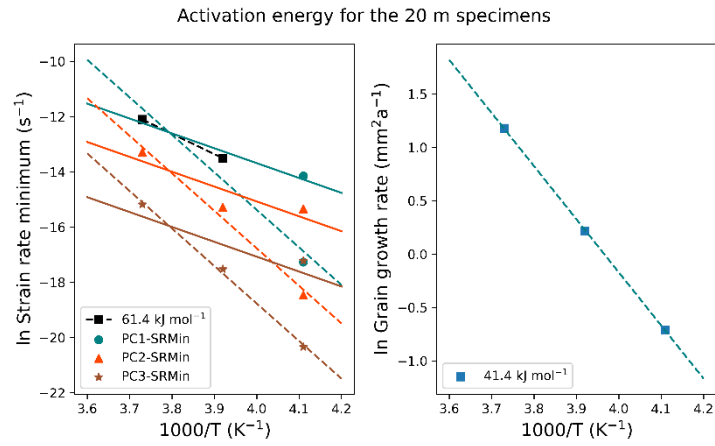
506

507

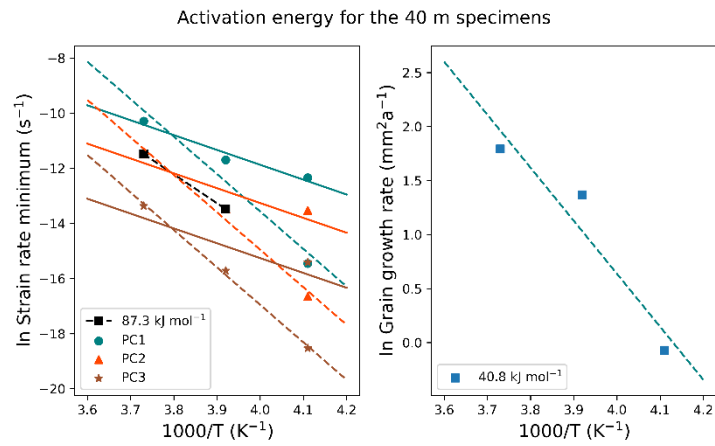
508 A great challenge is the estimation of the Q_c using the SRmin including the -30°C specimens,
509 whose SRmin shows high variability due to the extraordinarily slow strain rate at low
510 temperatures. This difficulty cannot be resolved by extrapolating experimental data (Sinha, 1978;
511 Hooke et al., 1980), e.g. the use of Andrade's law (Glen, 1955). Instead, we turned our focus to
512 studying the relationship between the SRmin and temperature by constraining our data in a wide
513 range of Q_c values reported in existing literature presented in **Table 4**. Clearly, there is a larger
514 scatter of Q_c values for firn than for ice. The increase of Q_c from mono-crystalline and
515 bi-crystalline to polycrystalline ice implies that the greater the reduction in the constraint from
516 grain boundaries, the greater is Q_c . Alternatively, firn creep is easier than that of polycrystalline
517 ice due to either the easier sliding of grains in firn along more directions in the more porous and
518 heterogeneous structure (Section 3.3), or the decrease of viscosity associated with inclusions (e.g.

519

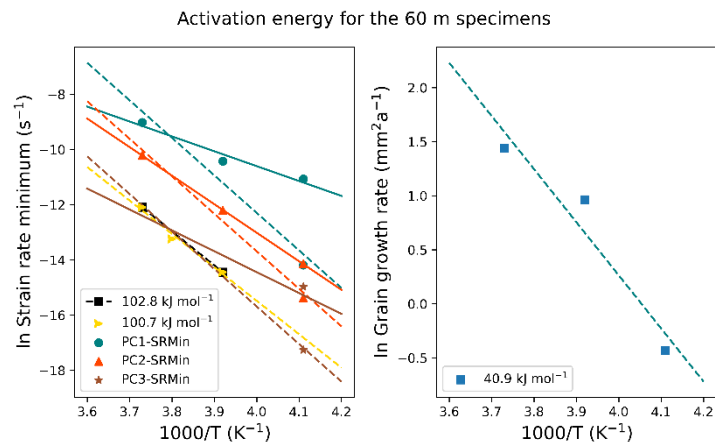
520



521



522



523

524

525

526

527

Figure 7: Arrhenius plots to estimate the apparent activation energy of creep (Q_c ; left panel) and the apparent activation energy of grain-boundary diffusion (Q_{gbd} ; right panel) from the firm specimens noted. The teal, orange, and brown solid lines are the upper bound (44.8 kJ mol⁻¹) of PC1-SRmin, PC2-SRmin, and PC3-SRmin, respectively, while the teal, orange, and brown dashed

528 lines are the lower bound (113 kJ mol⁻¹) of PC1-SRmin, PC2-SRmin, and PC3-SRmin,
529 respectively (Table 2). The teal circles, the orange triangles, and the brown stars are the data in
530 Table 2. The black dashed lines are from *only* two SRmins at -5°C and -18°C (the black squares
531 are the data measured), whose Q_c is indicated in each subfigure. The yellow dashed line is from
532 the three SRmins at -5°C, -18°C in this work, and -10 °C from Li and Baker (2022a) (the yellow
533 triangles are the measured data), whose Q_c is 110.7 kJ mol⁻¹. The blue dashed lines (right panel)
534 are from grain growth rate at three temperatures (the blue squares are the observed data), whose
535 Q_{gbd} is indicated in each subfigure.

536

537

538 Table 4. Apparent activation energy for the creep of firn and ice, Q_c , reported in literature.

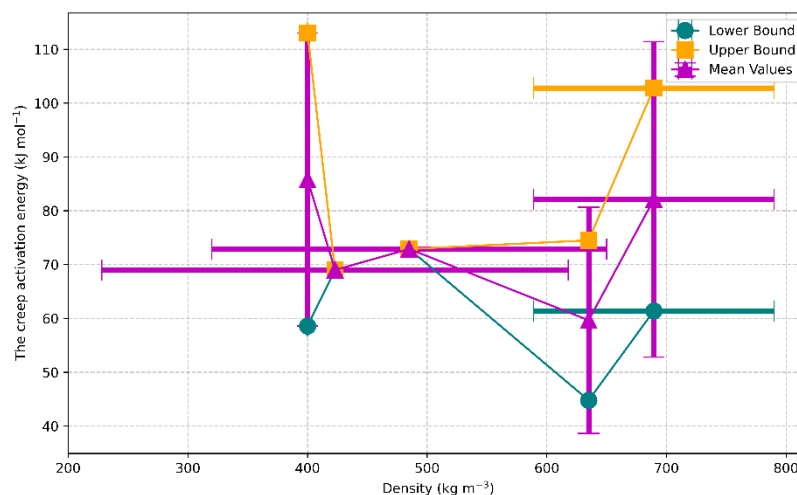
Q_c kJ mol ⁻¹	Sample	Density kg m ⁻³	Temperature °C	Methods	Source
58.6–113	Firn	~400	[-13.6, -3.6]	Uniaxial/Hydrostatic Compression	Landauer (1958)
44.8–74.5	Firn/Bubbly Ice	440–830	[-34.5, -0.5]	Uniaxial Unconfined Compression	Mellor and Smith (1966)
54	Firn/Bubbly Ice	Undetail ed	[-28, -16]	Shear Deformation of Boreholes	Paterson (1977)
~72.9	Firn	320–650	Unnecessary	Grain Growth Rate	Gow (1969)
69 ± 5	Firn	423 ± 8	[-19, -11]	Triaxial Compression	Scapozza and Bartelt (2003)
~60	Artificial/Natural Ice (South Pole)	~917	-15	Torsion Creep Test	Pimienta and Duval (1987)
61	Polycrystalline Ice	~917	-9.6	Hydrostatic Pressure	Duval et al. (1983)
78	Monocrystalline Ice	~917	[-30, -4]	Derived from Bicrystal Ice	Homer and Glen (1978)
75	Ice Bicrystal	~917	[-30, -4]	Tensile Test Parallel to Grain-boundary	Homer and Glen (1978)

539

540

541 Baker and Gerberich, 1979; Goodman et al., 1981) that facilitate the intra- and inter-grain sliding
542 (Salamatin et al., 2009). In principle, Q_c of firm should exceed that for polycrystalline ice.
543 Intriguingly, some reported Q_c values from firm are less than that for ice, meaning the degree of
544 spatial freedom in the ice-matrix is limited by the topological structure of the firm (Liu et al.,
545 2022). Incidentally, the effective stress of porous materials is determined by not only its porosity,
546 but also other factors, e.g. the microstructural topology (Liu et al., 2022) and the impurity types
547 and concentrations in the firm. However, this issue is beyond the scope of this work. In seeking a
548 conclusion, we evaluated the dependence of creep activation energy on firm density. The data
549 indicate no discernible relationship between these two parameters (Fig. 8). In summary, a Q_c for
550 firm, which ranges from 44.8–113 kJ mol⁻¹, is plausible due to the intrinsic nature of natural firm
551 that has a far more complicated and changeable microstructure than ice.

552



553

554 **Figure 8:** Plots of the creep activation energy vs. firm densities. For each density, three values are
555 shown: the lower bound (minimum activation energy, teal), the upper bound (maximum activation
556 energy, orange), and the mean value (magenta). Error bars represent the standard deviation of the

557 mean. Data are sourced from Table 4 and the present study.

558

559

560 The value of the stress exponent n is determined by plotting the line fit the logarithm relation of
561 the steady-state strain rate, $\dot{\epsilon}$, versus the effective stress, σ , and is, thus, the slope of this line
562 from the measured SRmins (**Table 2**). We determined stress exponent (n) values of approximately
563 0.1 and -1.2 for the -5°C and -18°C samples based on observed data, respectively. This result
564 directly contradicts the value of $n \approx 4.3$ reported from the same Greenland firn core by Li and
565 Baker (2022a). Further, these values fall entirely outside the established range of ~ 1 to ~ 7.5
566 (mean $\sim 4.25 \pm 3.25$) documented across decades of ice mechanics literature (Glen, 1955; Hansen
567 and Landauer, 1958; Butkovich and Landauer 1960; Kamb, 1961; Paterson and Savage, 1963;
568 Higashi et al, 1965; Mellor and Testa, 1969; Raymond, 1973; Hooke, 1981; Thomas et al., 1980;
569 Duval et al., 1983; Weertman, 1983,1985; Azuma and Higashi, 1984; Pimienta and Duval, 1987;
570 Budd and Jacka, 1989; Jacka and Li, 1994; Goldsby and Kohlstedt, 2001; Bindschadler et al.,
571 2003; Cuffey, 2006; Chandler et al. 2008; Cuffey and Kavanaugh, 2011; McCarthy et al., 2017;
572 Millstein et al., 2022; Colgan et al., 2023; Li, 2025). The wide range of reported n -values is
573 governed by a complex interplay of deformation mechanisms—including grain boundary sliding,
574 diffusion (lattice and grain boundary), and dislocation processes, e.g. hard-slip-dominated,
575 dislocation-accommodated grain boundary sliding, and grain boundary sliding-limited basal
576 dislocation—across varying stresses, temperatures, crystallographic fabrics, impurity contents, and
577 grain-size-to-sample-size ratios. We attribute the significant discrepancy in these findings to the
578 experimental conditions. The lower temperatures used (down to -30°C) induce slower strain rates,

579 which prevented the tests from reaching a critical strain rate minimum (SRMin). Therefore, to
580 accurately estimate the activation energy for deformation, it is necessary first to calibrate the
581 SRMin value for all noised samples. A constant stress exponent value of $n \approx 4.3$ (Li and Baker,
582 2022a) was used to compute the activation energy. This necessary simplification—an
583 acknowledgement of current methodological limitations rather than a dismissal of the underlying
584 physics—introduces a key uncertainty that highlights the need for future advancements in
585 observational methodology within firm research. To proceed, the post-calibration SRmins for the –
586 5°C and –18°C samples are highlighted in **Table 2** (see **Appendix B** in detail). It is important to
587 note that the stress exponent does not depend on the density of the tested samples, thereby
588 negating any basis for discussing a relationship between the stress exponent and sample density.
589 Instead, variations in stress corresponding to density variations are manifested in the strain rate,
590 ensuring that the derivation of the stress exponent and activation energy remains consistent. From
591 here on we only discuss the applied stress since there is little difference between the effective
592 stress and applied stress for calculating the stress exponent (Li and Baker, 2022a). Based on both
593 the reported range of Q_c and the two observed SRmins at –5°C and –18°C, the SRmins for the
594 –30°C samples are inferred (**Table 2**), using the Arrhenius relation. Also, based on both the
595 observed and inferred SRmins with the upper and lower bounds (**Table 2**), a series of fitted
596 functions are then found between the SRmin and the reciprocal of the temperature (°C), $1/T_c$:

597

598 20-m samples:

$$\left\{ \begin{array}{l}
\text{SRMin} = -3 \times 10^{-5} / T_c - 7 \times 10^{-7} [R^2 = 0.988; \text{PC 1(L 20)}] \\
\text{SRMin} = -3 \times 10^{-5} / T_c - 2 \times 10^{-7} [R^2 = 1; \text{PC 1(U 20)}] \\
\text{SRMin} = -1 \times 10^{-5} / T_c - 3 \times 10^{-7} [R^2 = 1; \text{PC 2(L 20)}] \\
\text{SRMin} = -9 \times 10^{-6} / T_c - 2 \times 10^{-7} [R^2 = 0.987; \text{PC 2(U 20)}] \\
\text{SRMin} = -2 \times 10^{-6} / T_c - 6 \times 10^{-8} [R^2 = 0.998; \text{PC 3(L 20)}] \\
\text{SRMin} = -1 \times 10^{-6} / T_c - 3 \times 10^{-8} [R^2 = 0.976; \text{PC 3(U 20)}]
\end{array} \right.$$

40-m samples:

$$\left\{ \begin{array}{l}
\text{SRMin} = -2 \times 10^{-4} / T_c - 4 \times 10^{-6} [R^2 = 0.988; \text{PC 1(L 40)}] \\
\text{SRMin} = -2 \times 10^{-4} / T_c - 2 \times 10^{-6} [R^2 = 1; \text{PC 1(U 40)}] \\
\text{SRMin} = -6 \times 10^{-5} / T_c - 2 \times 10^{-6} [R^2 = 1; \text{PC 2(L 40)}] \\
\text{SRMin} = -6 \times 10^{-5} / T_c - 1 \times 10^{-6} [R^2 = 0.987; \text{PC 2(U 40)}] \\
\text{SRMin} = -1 \times 10^{-5} / T_c - 3 \times 10^{-7} [R^2 = 0.998; \text{PC 3(L 40)}] \\
\text{SRMin} = -9 \times 10^{-6} / T_c - 2 \times 10^{-7} [R^2 = 0.976; \text{PC 3(U 40)}]
\end{array} \right.$$

60-m samples:

$$\left\{ \begin{array}{l}
\text{SRMin} = -7 \times 10^{-4} / T_c - 2 \times 10^{-5} [R^2 = 0.988; \text{PC 1(L 60)}] \\
\text{SRMin} = -6 \times 10^{-4} / T_c - 6 \times 10^{-6} [R^2 = 1; \text{PC 1(U 60)}] \\
\text{SRMin} = -2 \times 10^{-4} / T_c - 7 \times 10^{-6} [R^2 = 1; \text{PC 2(L 60)}] \\
\text{SRMin} = -2 \times 10^{-4} / T_c - 4 \times 10^{-6} [R^2 = 0.987; \text{PC 2(U 60)}] \\
\text{SRMin} = -3 \times 10^{-5} / T_c - 1 \times 10^{-6} [R^2 = 0.998; \text{PC 3(L 60)}] \\
\text{SRMin} = -3 \times 10^{-5} / T_c - 7 \times 10^{-7} [R^2 = 0.976; \text{PC 3(U 60)}]
\end{array} \right.$$

where PC1(L20) and PC1(U20) indicate the lower and upper bound values of the post-calibration SRmins from the 20 m samples (**Table 1**), and other symbols are similarly formatted, e.g. PC1(L40), PC1(U40), PC1(L60), PC1(U60), and so on. These relationships are plotted in **Figure 8**, where the SRmin vs. $1/T_c$ plots from the three depths are almost the same shape, implying that the SRmin is dependent on the temperature at a constant stress. It is important to note that the average (minimum) strain rate for the secondary creep stage for a given temperature increases with increasing depth/density of the samples (**Figure 8; Table 2**). This is opposite to a decrease of

612 the SRmin at a fixed stress and temperature in **Figure 8** and **Table 4** in Li and Baker (2022a).
613 These changes in SRmin are irrespective of the stress (**Appendix A**). The temperature plays a
614 predominant role during firm creep for a given density of sample at a constant stress. An
615 interesting question on firm creep at a specific temperature is whether the SRmin slows down or
616 speeds up with decreasing density of firm. Certainly, natural firm samples raise the complexity in
617 interpreting the firm creep due to the influences both from inclusions (Li and Baker, 2022a and
618 references therein; Li, 2024), and from the topology of the microstructures (Liu et al., 2022). In
619 addition, there is a broad spread of the SRmin at each depth, in which the SRmin varies by several
620 times, even one order of magnitude or more between the different possibilities of post-calibration
621 SRmins (**Figure 8**), implying that the microstructure of the sample significantly influences the

622

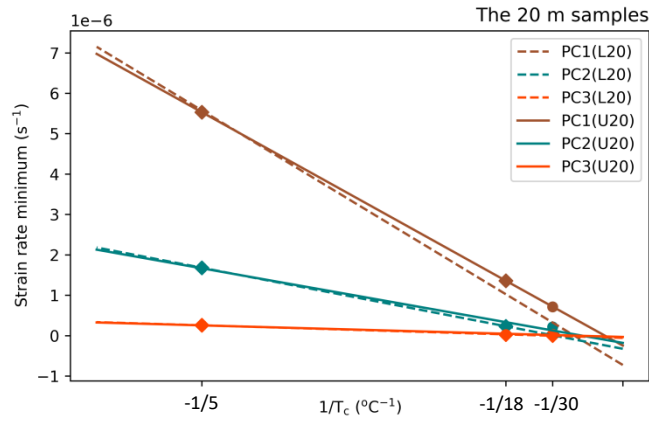
623

624

625

626

627



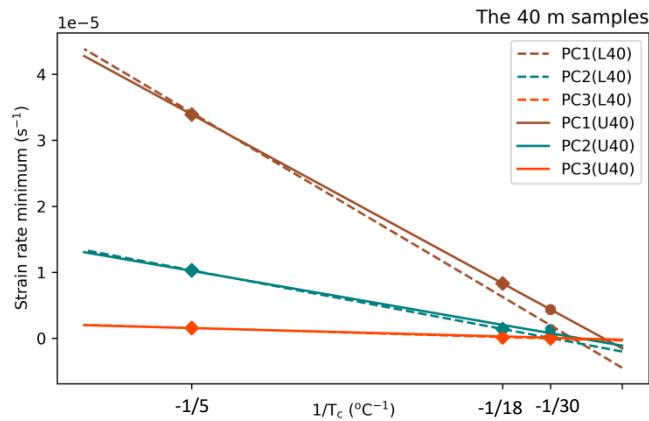
628

629

630

631

632



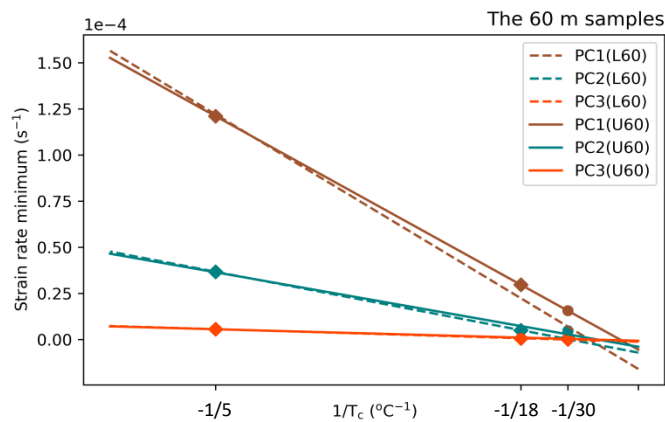
633

634

635

636

637



638 **Figure 9:** Plots of the strain rate minimum versus the reciprocal of temperature. PC1(L20) and

639 PC1(U20) indicates the lower and upper bound, respectively, from the 20 m samples via PC1 as

640 noted in Table 2, and so on. The circles indicate the upper bound data measured and inferred,

641 while the squares indicate the lower bound data. The dashed line is the fit from the lower bound,

642 while the solid line is the fit from the upper bound.

643

644

645 process of the creep of firn. Moreover, it is hard to generalize a universal formula for predicting
646 the SRmin at temperatures below -30°C , where the SRmins becomes negative (**Figure 8**). Thus,
647 there is a need for an in-depth understanding of the polar firn creep behavior in secondary creep
648 stage.

649

650 To illustrate the differences between the Q_c values calculated from PC1-SRmin, PC2-SRmin,
651 and PC3-SRmin, we have plotted them in **Figure 7**. Interestingly, the Arrhenius plots of the
652 natural logarithm of strain rate with $1000/T$ (**Figure 7**) are similar to those observed by Glen
653 (1955) and Homer and Glen (1978), implying that there is no significant difference in the creep
654 mechanism for a temperature range of -30°C to -5°C (Glen, 1955; Homer and Glen, 1978),
655 where both diffusion via grain-boundary, vacancy or interstitial defects (Barnes et al., 1971;
656 Brown and George, 1996; Nasello et al., 2005; Li and Baker, 2022b), and dislocations contribute
657 to the creep of polar firn.

658

659 **4. Conclusions**

660 Constant-load creep tests were performed on three cylindrical specimens tested from depths of 20
661 m (applied stress 0.21 MPa), 40 m (0.32 MPa) and 60 m (0.43 MPa) at temperatures of $-5 \pm$
662 0.2°C , $-18 \pm 0.2^{\circ}\text{C}$, and $-30 \pm 0.2^{\circ}\text{C}$ from a firn core extracted at Summit, Greenland in June
663 2017. The microstructures were characterized before and after creep testing using the micro-CT
664 and thin sections viewed between optical crossed polarizers. It was found that:

665

- 666 1. Microstructural parameters measured using the micro-CT show that the polar firn densified
667 during the creep compression (e.g. from 685 to 729 kg m⁻³ for the 40 m specimen at -5°C),
668 viz., the TP (from 25.5 to 20.7%), the ECDA (from 0.86 to 0.69 mm), the SSA (from 3.26 to
669 3.02 mm⁻¹), and the SMI (from -1.85 to -2.8) decreased, while the S.Th (from 0.95 to 0.99
670 mm) and the CP (from 0.01 to 0.02%) increased. Anomalies in the microstructures, especially
671 at low temperatures of -18°C and -30°C, are likely due to metamorphism under temperature
672 gradients, the radial dilation effect during firn deformation, the measurement uncertainty of
673 the micro-CT, or the anisotropy and the heterogeneity of natural firn.
- 674 2. The transient creep behavior of firn at constant stress and different temperatures obeys an
675 Andrade-like law, but, the time exponent k of 0.34–0.69 is greater than the 0.33 found for ice.
676 This is due to fewer grain-boundary constraints in porous firn than in ice.
- 677 3. The secondary creep behavior of firn at constant stress and different temperatures presented
678 here shows that the strain at the SRmin increases with decreasing firn density and increasing
679 creep temperature. In particular, low-density firn during creep at high temperatures shows that
680 the strain at the SRmin, e.g. 11.8% and 7.5% respectively from the 20 m and 40 m specimens
681 at -5°C, is greater than the strain of 3%, which is the maximum found at the SRMin of ice.
- 682 4. The tertiary creep behavior of firn at constant stress and different temperatures is more easily
683 observed from lower-density specimens at greater effective stresses and higher creep
684 temperatures. The strain softening in tertiary creep is primarily due to recrystallization.
- 685 5. The apparent activation energy for the firn creep has a wide range of 61.4–102.8 kJ mol⁻¹
686 because the grains in firn slide more easily along more directions in the more porous and
687 heterogeneous structure, the enhanced fluidity from inclusions, and the topological structure

688 of the firn. In addition, the SR_{min} is a function of the temperature, depending on the
689 microstructure of firn and the inclusion content. The predicted SR_{min} increases with
690 increasing firn density at a given temperature and is independent of the effective stress. Lastly,
691 there is no significant difference in the creep mechanism at temperatures ranging from $-30^{\circ}C$
692 to $-5^{\circ}C$.

693

694 The creep of polar firn behaves differently from full-density ice, implying that firn densification is
695 an indispensable process in fully understanding the transformation of snowfall to ice in the polar
696 regions. Observed firn deformation indicates that temperature plays a determined role in firn
697 densification. Thereby, it will be helpful to bridge a gap between the firn temperature and the
698 climate of the past for reconstructing paleoclimate. Also, it will be helpful to apply a confining
699 load to investigate the microstructure of the creep of polar firn with smaller initial particle sizes at
700 low temperatures using the micro-CT. Further studies of interest are to investigate the quantitative
701 relationship between the microstructural parameters and the mechanical behavior of polar firn,
702 and when the onset of recrystallization occurs during creep, as well as verify the SR_{min} predicted
703 by the relationship of SR_{min} vs. temperature from the firn specimens at more extensive ranges of
704 stresses and temperatures.

705 **Appendix A:** Hydrostatic pressure, the applied stress, and the effective stress

706 The hydrostatic pressure, p , which varies with temperature, along with the cohesion of the ice and
707 the friction angle between snow particles, plays a significant role in determining the apparent
708 activation energy and, consequently, the strength of the ice (Fish, 1991). It was calculated from
709 the overburden pressure of snow, i.e. $p = \bar{\rho}_f g h$, where $\bar{\rho}_f$ is the average firm density above the
710 depth of interest, h , and g is the acceleration of gravity. At Summit, p at the depths of 20 m, 40 m,
711 and 60 m was estimated to be ~ 0.1 MPa, ~ 0.22 MPa, and ~ 0.38 MPa, respectively. Note that the
712 slope of the surface of ice sheets and glaciers at Summit is idealized to be zero, i.e., their surfaces
713 are horizontal. The applied stress, σ , is the applied load divided by the cross-sectional area of a
714 sample. The σ at the depths of 20 m, 40 m, and 60 m were 0.21 MPa, 0.32 MPa, and 0.43 MPa,
715 respectively. The effective stress, $\tilde{\sigma}$, is defined as σ divided by the fraction of ice matrix in
716 firm, see in detail from Li and Baker (2022a). Thereby, $\tilde{\sigma}$ is 0.32 MPa (the mean porosity of
717 34.9%), 0.43 MPa (24.8%), and 0.5 MPa (14.4%) from the 20–60 m samples, respectively. Note
718 that the stresses were vertically loaded on the sample (parallel to the direction of core axis of the
719 sample) in laboratory tests. Ideally, in order to be analogous to the densification of firm in nature,
720 $\tilde{\sigma}$ for laboratory samples from a given depth should be equal to the p of firm *in situ* at an
721 equivalently same depth at Summit, namely $\tilde{\sigma}/p = 1$. However, in consideration of the laboratory
722 timeframe for experiments (Pimienta and Duval, 1987), the stresses applied in laboratory tests are
723 usually higher with a resulting higher rate of deformation than those *in situ*. Thus, to observe the
724 effect of the stress on the creep of firm with different densities at different depths, we designed the
725 following configuration of the $\tilde{\sigma}/p$ with depth, viz., $0.32 \text{ MPa}/\sim 0.1 \text{ MPa} = \sim 3.2$, $0.43 \text{ MPa}/\sim 0.22$
726 $\text{MPa} = \sim 1.95$, and $0.5 \text{ MPa}/\sim 0.38 \text{ MPa} = \sim 1.32$ for the samples from the depths of 20 m, 40 m,

727 and 60 m, respectively. In this manner, the decrement of $\tilde{\sigma}/p$ with increasing depth represents
728 the decrease of the effective stress with increasing depth. Also, it's important to note that the
729 strain rates achieved during creep experiments in laboratory settings are 6 to 7 times faster than
730 on ice sheets due to the constraints of conducting experiment in reasonable times, which requires
731 higher loads.

732

733 **Appendix B:** Strain rate minimum inferred via two kinds of constraints

734 To improve the reliability of inferred SRmins, two kinds of constraints were applied. First, the
735 SRmins from the -5°C and -18°C samples are calibrated using Glen's law $\dot{\epsilon}=A\sigma^n$ with $n = 4.3$
736 (Li and Baker, 2022a). PC1-SRmin, PC2-SRmin, and PC3-SRmin indicate three possibilities of
737 the SRmins that are calculated from the 20 m, 40 m, and 60 m samples via the *only* SRmin
738 observed at a given temperature (Table 2). As an example, for the -5°C samples, there exist three
739 possibilities from three depths. 1) The SRmin observed from the 20 m sample in bold italic font is
740 used to calculate two other SRmins for the 40 m and 60 m samples in the italic font in the column
741 of PC1-SRmin. 2) In the same manner as in scenario 1), the SRmin observed from the 40 m
742 sample is calculated in the column of PC2-SRmin in the bold italic font, and the SRmin observed
743 from the 60 m sample is calculated in the column of PC3-SRmin in the bold italic font. 3) In the
744 same manner as in scenarios 1) and 2), the SRmin is calculated for the -18°C samples in turn
745 from three depths. Second, the SRMin of the -30°C samples is inferred on the basis of the range
746 of Q_c , i.e., from 44.8 kJ mol^{-1} (upper bound) to 113 kJ mol^{-1} (lower bound), using the Arrhenius
747 relation.

748 **Data availability**

749 The data supporting the conclusions in this study are available at <https://arcticdata.io/catalog>.

750

751 **Author contribution**

752 Y.L. and I.B. designed the experiments and Y.L. carried them out. Y.L. analyzed the data and
753 visualized the relevant results. Y.L. prepared the manuscript with contributions from all
754 co-authors (K.K. and I.B.).

755

756 **Competing interests**

757 At least one of the (co-)authors is a member of the editorial board of The Cryosphere.

758

759 **Acknowledgements**

760 This work was sponsored by the National Science Foundation under Arctic Natural Science Grant
761 No. 1743106. Y.L. gratefully acknowledges Ciao Fu for her great support and help in during the
762 COVID-19 pandemic. The authors wish to thank Chris Polashenski, Zoe Courville and Lauren B.
763 Farnsworth at USA-CRREL for their assistance with the storage of the firm cores. We also
764 acknowledge the use of facilities of the Ice Research Laboratory (Director-Erland Schulson) at
765 Dartmouth College. Finally, the authors thank Editor Nanna Bjørnholt Karlsson, Louis Védrine
766 and an anonymous reviewer for their constructive comments, which significantly improved the
767 quality of this manuscript.

768 **References:**

- 769 Adolph, A.C.C., Albert, M.R., 2014. Gas diffusivity and permeability through the firn column at
770 Summit, Greenland: measurements and comparison to microstructural properties. *T.*
771 *Cryosph.*, 8, 319–328, doi:10.5194/tc-8-319-2014.
- 772 Albert, M.R., Shultz, E.F. and Perron, F.E., 2000. Snow and firn permeability at Siple Dome,
773 Antarctica. *Ann. Glaciol.* 31, 353-356.
- 774 Alley, R.B., Clark, P.U., Huybrechts, P., Joughin, I., 2005. Ice-sheet and sea-level changes. *Sci.*
775 310(5747), 456-60. doi: 10.1126/science.1114613. PMID: 16239468.
- 776 Ambach, W., Eisner, H., 1985. Rheological properties of temperate firn. *Polarforschung*,
777 Bremerhaven, Alfred Wegener Institute for Polar and Marine Research & Germany Society
778 of Polar Research 55(2), 71–77. hdl:10013/epic.29564.d001.
- 779 Anderson, D.L., Benson, C.S., 1963. The densification and diagenesis of snow. In: Kingery, W.D.
780 (Ed.), *Ice and Snow*. Press, Cambridge, Massachusetts, M.I.T, pp. 391–411.
- 781 Arnaud, L., Gay, M., Barnola, J.M., Duval P., 1998. Imaging of firn and bubbly ice in coaxial
782 reflected light: a new technique for the characterization of these porous media. *J. Glaciol.*,
783 44(147), 326-332.
- 784 Ashby, M.F., Duval, P. 1985. The creep of polycrystalline ice. *Cold Reg. Sci. Technol.*, 11 (3),
785 285-300. doi:10.1016/0165-232X(85)90052-7.
- 786 Azuma, N., Higashi, A., 1984. Mechanical properties of Dye 3 Greenland deep ice cores. *Ann.*
787 *Glaciol.*
- 788 Baker, R.W., Gerberich, W.W., 1979. The effect of crystal size and dispersed-solid inclusions on
789 the activation energy for creep of ice. *J. Glaciol.*, 24(90), 179-194.

- 790 Barnes, P., Tabor, D., Walker, J.C.F., 1971. The friction and creep of polycrystalline ice. Proc. Roy.
791 Soc. Lond. A (324),127-155.
- 792 Bartelt, P., Von Moos, M., 2000. Triaxial tests to determine a microstructure-based snow viscosity
793 law. Ann. Glaciol., 31, 457-462.
- 794 Bindschadler, R., King, M., Alley, R., Anandakrishnan, S., Padman, L., 2003. Tidally controlled
795 stick-slip discharge of a West Antarctic ice stream. Ann. Glaciol., 36, 157–162.
- 796 Brown, D.E., George, S.M., 1996. Surface and bulk diffusion of H₂¹⁸O on single-crystal H₂¹⁶O ice
797 multilayers. J. Phys. Chem. 100 (38) 15460–15469.
- 798 Budd, W.F., Jacka, T.H., 1989. A review of ice rheology for ice sheet modelling. Cold Reg. Sci.
799 Technol. 16(2), 107–144. doi: 10.1016/0165-232X(89)90014-1.
- 800 Burr, A., Ballot, C., Lhuissier, P., Martinerie, P., Martin, C.L., Philip, A., 2018. Pore morphology
801 of polar firn around closure revealed by X-ray tomography, T. Cryosph., Copernicus, 12(7),
802 2481-2500. 10.5194/tc-12-2481-2018. hal-01864373.
- 803 Butkovich, T.R., Landauer, J.K., 1960. Creep of ice at low stresses. U.S. Snow, Ice and
804 Permafrost Research Establishment. Research Report 72.
- 805 Chandler, D., B. Hubbard, A. Hubbard, T. Murray, Rippin, D., 2008. Optimising ice flow law
806 parameters using borehole deformation measurements and numerical modelling. Geophys.
807 Res. Lett., 35, L12502.
- 808 Chen, M., Chen, Z.D., 1997. Effective stress laws for multi-porosity media. Appl. Math. Mech.,
809 20(11), 1207–1213.
- 810 Coleou, C., Lesaffre, B., Brzoska, J.B., Ludwig, W., Boller, E., 2001. Three-dimensional snow
811 images by X-ray microtomography, Ann. Glaciol., 32, 75-81.

812 Colgan, W., et al., 2023. Sixty years of ice form and flow at Camp Century, Greenland. *J. Glaciol.*,
813 69(276), 919–929.

814 Courville, Z., Horhold, M., Hopkins, M. and Albert, M., 2010. Lattice-Boltzmann modeling of the
815 air permeability of polar firn. *J. Geophys. Res., Earth Surface*, 115(F4).

816 Coussy, O., 2004. *Poromechanics*. John Wiley & Sons.

817 Cuffey, K.M., 2006. Manifestations of ice microphysical processes at the scale of whole ice sheets.
818 In: Knight, P. (Ed.), *Glacier Science and Environmental Change*. Blackwell Publishing, 290–
819 300.

820 Cuffey, K.M., Paterson, W.S.B., 2010. *The Physics of Glaciers*, 4th edited. Elsevier Inc.

821 Cuffey, K.M., Kavanaugh, J.L., 2011. How nonlinear is the creep deformation of polar ice? A new
822 field assessment. *Geol.*, 39(11), 1027–1030.

823 da Silva, M.R., Schroeder, C., Verbrugge, J.C., 2008. Unsaturated rock mechanics applied to a
824 low-porosity shale. *Eng. Geol.*, 97, 42–52.

825 Durham, W.B., Stern, L.A., 2001. Rheological properties of water ice applications to satellites of
826 the outer planets. *Annu. Rev. Earth Planet. Sci.* 29(1), 295–330.

827 Duval, P., 1981. Creep and fabrics of polycrystalline ice under shear and compression. *J. Glaciol.*
828 27, 129–140.

829 Duval, P. Ashby, M.F., Anderman, I., 1983. Rate-controlling processes in the creep of
830 polycrystalline ice. *The Journal of Physical Chemistry*, 87, 4066-4074.

831 Duval, P., Montagnat, M., 2002. Comment on ‘Superplastic deformation of ice: experimental
832 observations’ by D. L. Goldsby and D. L. Kohlstedt. *J. Geophys. Res.: Solid Earth*. 107(B4),
833 ECV 4-1–ECV 4-2. doi: 10.1029/2001JB000946.hal-01698732.

834 Ebinuma, T., Maeno, N., 1987. Particle rearrangement and dislocation creep in a snow
835 densification process. *J Phys.(Paris)*, 48,Colloq. C1, 263–269.

836 Ehlers, W., 2002. Foundations of multiphasic and porous materials. In Ehlers Wolfgang and
837 Bluhm J eds. Porous Media– Theory, Experiments and Numerical Applications. Berlin:
838 Springer, pp. 3–86.

839 Eichler, J., 7 others, 2017. Location and distribution of micro-inclusions in the EDML and NEEM
840 ice cores using optical microscopy and in situ Raman spectroscopy. *The Cryosphere*. 11(3),
841 1075–1090. doi: 10.5194/tc-11-1075-2017.

842 Faria, S.H., Weikusat, I., Azuma, N., 2014. The microstructure of polar ice. Part II: state of the art.
843 *J. Struct. Geol.* 61, 21–49. doi:10.1016/j.jsg.2013.11.003.

844 Fish, A.M. (1991) Creep and yield model of ice under combined stress. USA Cold Regions
845 Research and Engineering Laboratory, Special Report 91-31.

846 Flin, F., Brzoska, J.B., Lesaffer, B., Coleou, C., Pieritz, R.A., 2004. Three-dimensional geometric
847 measurements of snow microstructural evolution under isothermal conditions. *Ann. Glaciol.*,
848 38, 39-44.

849 Freitag, J., Dobrindt, U., Kipfstuhl, J., 2002. A new method for predicting transport properties of
850 polar firm with respect to gases on the pore-space scale, *Ann. Glaciol.*, 35, 538-544.

851 Frost, H.J., Ashby, M.F. 1982. Deformation-mechanism maps: the plasticity and creep of metals
852 and ceramics. Oxford: Pergamon Press.

853 Fujita, S., Hirabayashi, M., Goto-Azuma, K., Dallmayr, R., Satow, K., Zheng, J., Dahl-Jensen, D.,
854 2014. Densification of layered firm of the ice sheet at NEEM, *J. Glaciol.*, 60 (223), 905-921,
855 doi:10.3189/2014JoG14J006.

856 Gagliardini, O., Meyssonier, J., 2000. Simulation of the creep of ice with a self-consistent
857 anisotropic approach. *Comput. Mech.*, 25(5), 479-486.

858 Glen, J.W., 1955. The creep of polycrystalline ice, *Proceedings of the Royal Society A*, 228(1175),

859 519-538, doi.10.1098/rspa.1955.0066.

860 Goldsby, D.L., Kohlstedt, D.L., 1997. Grain boundary sliding in fine-grained ice I. *Scr. Mater.*
861 37(9), 1399–1406.

862 Goldsby, D.L., Kohlstedt, D.L., 2001. Superplastic deformation of ice: experimental observations,
863 *J. Geophys. Res.*, 106(B6), 11017-11030.

864 Goodman, D.J., Frost, H.J., Ashby, M.F., 1981. The plasticity of polycrystalline ice, *Philos. Mag.*,
865 A43 665–695.

866 Gow, A.J., 1969. On the rates of growth of grains and crystals in South Polar firn. *J. Glaciol.*, 8(53)
867 241-252.

868 Gray, W.G., Schrefler, B.A., 2007. Analysis of the solid stress tensor in multiphase porous media.
869 *Int. J. Numer. Anal. Methods Geomech.*, 31, 541–581.

870 Gubler, H., 1978. Determination of the mean number of bonds per snow grain and of the
871 dependence of the tensile strength of snow on stereological parameters. *J. Glaciol.*,
872 20(83),329-341.

873 Hammonds, K., Baker, I., 2016. The effects of Ca⁺⁺ on the strength of polycrystalline ice. *J.*
874 *Glaciol.* 62,1–9. doi: 10.1017/jog.2016.84.

875 Hammonds, K., Baker, I., 2018. The effects of H₂SO₄ on the mechanical behavior and
876 microstructural evolution of polycrystalline Ice. *J. Geophys. Res.: Solid Earth.* 123,1–22. doi:
877 10.1002/2017JF004335.

878 Hansen, B.L., Landauer, J.K., 1958. Some results of ice cap drill hole measurements. *IASH Publ.*
879 47 (Symposium at Chamonix 1958– Physics of the Movement of the Ice), 313–317.

880 Hansen, A.C., Brown, R.L., 1988. An internal state variable approach to constitutive theories for
881 granular materials with snow as an example. *Mech. Mater.*, 7(2),109-119.

882 Higashi, A., Konimua, S., Mae, S., 1965. Plastic yielding in ice single crystals. *Jpn. J. Appl. Phys.*
883 4, 575-82.

884 Hildebrand, T., Ruesegger, P. 1997. A new method for the model-independent assessment
885 of thickness in three-dimensional images. *J. Microsc.*, 185, 67-75.

886 Hobbs, P.V., 1974. *Ice Physics*, 1st edited. Oxford University Press Inc., New York.

887 Homer, D.R., Glen, J.W., 1978. The creep activation energies of ice. *J. Glaciol.*, 21(85), 429-444.

888 Hooke, R.L., Mellor, M., Budd, W.F., Glen, J.W., Higashi, A., Jacka, T.H., Jones, S.J., Lile, R.C.,
889 Martin, R.T., Meier, M.F., Russell-Head, D.S., Weertman, J., 1980. Mechanical properties of
890 polycrystalline ice: an assessment of current knowledge and priorities for research. *Cold Reg.*
891 *Sci. Technol.*, 3, 263-275.

892 Hooke, R.L., 1981. Flow law for polycrystalline ice in glaciers: comparison of theoretical
893 predictions, laboratory data, and field measurements. *Rev. Geophys. Space Phys.*, 19(4),
894 664-672.

895 Hooke, R.L., 2005. *Principles of Glacier Mechanics*. Cambridge: Cambridge University Press.

896 Horhold, M.W., 5 others, 2012. On the impact of impurities on the densification of polar firn.
897 *Earth Planet. Sci. Lett.* 325-326, 93-99. doi: 10.1016/j.epsl.2011.12.022

898 Hutter, K., Johnk, K., 2004. *Continuum Methods of Physical Modeling: Continuum Mechanics,*
899 *Dimensional Analysis, Turbulence*. Springer Science & Business Media.

900 Jacka, T.H. 1984. The time and strain required for development of minimum strain rates in ice.
901 *Cold Reg. Sci. Technol.*, 8 (3), 261-268. doi: 10.1016/0165-232X(84)90057-0.

902 Jacka, T.H., Li, J. 1994. The steady state crystal size of deforming ice. *Ann. Glacial.*, 20, 13-18.

903 Jacka, T.H., Li, J., 2000. Flow rates and crystal orientation fabrics in compression of
904 polycrystalline ice at low temperatures and stresses, *Physics of Ice Core Records*
905 *International Symposium on Physics of Ice Core Records*. Shikotsukohan, Hokkaido, Japan,

906 83-102.

907 Jonas, J.J., Muller, F., 1969. Deformation of ice under high internal shear stresses. *Can. J. Earth*
908 *Sci.* 6(4), 963–968. doi: 10.1139/e69-100.

909 Jumawan, A.B., 1972. An experimental study of self-diffusion in polycrystalline ice. *Diss.Abstr.*
910 *Int. B* 32, 5163–5164 (Abstract).

911 Kamb, B., 1961. The thermodynamic theory of nonhydrostatically stressed solids. *J. Geophys.*
912 *Res.* 66, 259–271.

913 [Khalili, N., Geiser, F. Blight, G.E., 2004. Effective stress in un-saturated soils, a review with new](#)
914 [evidence. *Int. J. Geomech.*, 4\(2\), 115–126.](#)

915 King, R.F., 1952. Dissertation, Cambridge.

916 [Lade, P.V., Boer, R.V., 1997. The concept of effective stress for soil, concrete and rock. *Geotech.*,](#)
917 [47\(1\), 61–78.](#)

918 Landauer, J.K., 1958. The creep of snow under combined stress. *Transactions of the society of*
919 *rheology* II. 175-194.

920 Li, J., Jacka, T.H., Budd, W.F., 1996. Deformation rates in combined compression and shear for
921 ice which is initially isotropic and after the development of strong anisotropy. *Ann. Glaciol.*,
922 23, 247-252.

923 Li, Y., Baker, I. 2021. Dynamic observations of the densification of polar firn under compression
924 using a micro-computed tomograph, *J. Geophys. Res., Earth Surface*,126, e2021JF006290.
925 doi:org/10.1029/2021JF006290.

926 Li, Y. 2022. Critical values of the microstructural parameters at the first critical density of the
927 densification of polar firn. *Cold Reg. Sci. Technol.*, 198(2022), 10355.
928 doi:org/10.1016/j.coldregions.2022.103553.

- 929 Li, Y., Baker, I. 2022a. Observations of the creep of polar firn. *J. Glaciol.*, 68(268), 269–287.
930 doi.org/10.1017/jog.2021.91.
- 931 Li, Y., Baker, I. 2022b. Metamorphism observation and model of snow from Summit, Greenland
932 under both positive and negative temperature gradients in a Micro CT, *Hydrol. Processes*,
933 e14696. [doi.10.1002/HYP.14696](https://doi.org/10.1002/HYP.14696).
- 934 Li, Y. 2023a. Are bubbles in ice the potential space for hydrogen storage? *Int. J. Hydrogen*
935 *Energy*, 50(D), 575-585. doi.org/10.1016/j.ijhydene.2023.07.273.
- 936 Li, Y. 2023b. Changes in grain size during the relaxation stage of viscoelastic firn, *Philos. Mag.*,
937 104(4), 239-259. doi.org/10.1080/14786435.2023.2296656.
- 938 Li, Y. Fu, C. Keegan, C. et al. 2023. Microstructural characterization of depth hoar and ice-crust
939 layers using a micro-CT, and hypothesis of ice-crust formation under a thunderstorm, *Hydrol.*
940 *Processes*, 37(12), e15060. doi.org/10.1002/hyp.15060.
- 941 Li, Y. 2024a. Hydrogen production via imperfective ice *Ih*. *Int. J. Hydrogen Energy*. 100, 727–
942 735.
- 943 Li, Y. 2024b. Hydrogen storage-learn from the air clathrate hydrate in polar ice sheets.
944 *Sustainable Energy Technol. Assess.* 72, 104007.
- 945 Li, Y. 2024c. The improvement of hydrogen storage capacity via bubbles nucleated in ice-like
946 nanotubes, *Mater. Today Sustainability*, 27, 100856.
- 947 Liu, K., Sun, R. & Daraio, C. 2022. Growth rules for irregular architected materials with
948 programmable properties. *Sci.*, 377(6609), 975-981.
- 949 Lundin, J.M., Stevens, C.M., Arthern, R., Buizert, C., Orsi, A., Ligtenberg, S.R., et al. 2017. Firn
950 model intercomparison experiment (FirnMICE). *J. Glaciol.* 63(239), 401–422.
951 <https://doi.org/10.1017/jog.2016.114>.
- 952 Maeno, N., Ebinuma, T., 1983. Pressure sintering of ice and its implication to the densification of
953 snow at polar glaciers and ice sheets. *J. Phys. Chem.* 87, 4103–4110.

- 954 Mahajan, P. and R.L. Brown. 1993. A microstructure-based constitutive law for snow. *Ann.*
955 *Glaciol.*,18, 287-294.
- 956 McCarthy, C., Savage, H., Nettles, M., 2017. Temperature dependence of ice-on-rock friction at
957 realistic glacier conditions. *J. Glaciol.*, 63(241), 595–606.
- 958 Mellor, M., Smith, J.H., 1966. Creep of snow and ice, CRREL Res. Rep. 220.
- 959 Mellor, M., Testa, R., 1969. Effect of temperature on the creep of ice. *J. Glaciol.*, 8(52), 131-145.
- 960 Mellor, M., 1975. A review of basic snow mechanics. *Int. Assoc. Hydrol. Sci.* 114, 251–291.
- 961 Meussen, B., Mahrenholtz, O., Oerter, H., 1999. Creep of polar firn. *Cold Reg. Sci. Technol.* 29,
962 177–200. doi: 10.1016/S0165-232X(99)00018-X
- 963 Millstein, J.D., Minchew, B.M., Pegler, S.S., 2022. Ice viscosity is more sensitive to stress than
964 commonly assumed. *Commun. Earth Environ.*, 3, 57.
- 965 Nasello, O.B., Di Prinzio, C.L., Guzman, P.G., 2005. Temperature dependence of “pure” ice grain
966 boundary mobility, *Acta Mater.*, 53(18) 4863-4869, doi: 10.1016/j.actamat.2005.06.022.
- 967 Nuth, M., Laloui, L., 2008. Effective stress concept in unsaturated soils: clarification and
968 validation of a unified framework. *Int. J. Numer. Anal. Methods Geomech.*, 32, 771–801.
- 969 Ogunmolasuyi, A., Murdza, A., Baker, I. 2023. The onset of recrystallization in polar firn.
970 *Geophys. Res. Lett.*, 50, e2023GL103435. doi.org/10.1029/2023GL103435.
- 971 Paterson, W.S.B., Savage, J.C., 1963. Measurements on Athabasca Glacier relating to the flow
972 law of ice. *J. Geophys. Res.*, 68:4537-43.
- 973 Paterson, W.S.B., 1977. Secondary and tertiary creep of glacier ice as measured by borehole
974 closure rates, *Rev. Geophys. Space Phys.*, 15, 47–55.
- 975 Perutz, M.F., Seligman, G., 1939. A crystallographic investigation of glacier structure and the
976 mechanism of glacier flow. *Proc. Roy. Soc. London A* 172, 335–360.

- 977 Petrenko, V.F., Whitworth, R.W., 1999. *Physics of Ice*. Oxford: Oxford University Press.
- 978 Pimienta, P., Duval, P., 1987. Rate controlling processes in the creep of polar glacier ice. *Journal*
979 *de Physique*, 48, 243-248.
- 980 Raymond, C.F., 1973. Inversion of flow measurements for stress and rheological parameters in a
981 valley glacier. *J. Glaciol.* 12, 19–44.
- 982 Salamatin, A.N., Lipenkov, V.Y., Barnola, J.M., Hori, A., Duval, P., Hondoh, T. 2009. Snow/firn
983 densification in polar ice sheets. In: Hondoh, T. (Ed.), III. *Firn densification, close-off and*
984 *chronology*, 195-222, Hokkaido University Press.
- 985 Salm, B., 1982. Mechanical properties of snow. *Rev. Geophys. Space Phys.*, 20(N1), 1–19.
- 986 Scapozza, C., Bartelt, P.A., 2003. The influence of temperature on the small-strain viscous
987 deformation mechanics of snow: a comparison with polycrystalline ice. *Ann. Glaciol.*, 37,
988 90–96.
- 989 Schleef, S., Lowe, H., Schneebeli, M., 2014. Influence of stress, temperature and crystal
990 morphology on isothermal densification and specific surface area decrease of new snow. *T.*
991 *Cryosphy.*, 8, 1825-1838.
- 992 Sinha, N.K., 1978. Short-term rheology of polycrystalline ice. *J. Glaciol.*, 21(85) 457-472.
- 993 Steinemann, S., 1954. Flow and recrystallisation of ice. *Proc. Int. Assoc. Hydrol. Sci.* 39, 449–
994 462.
- 995 Song, M., Baker, I., Cole, D.M., 2005. The effect of particles on dynamic recrystallization and
996 fabric development of granular ice during creep. *J. Glaciol.* 51(173), 377–382. doi:
997 10.3189/172756505781829287.
- 998 Song, M., Cole, D.M., Baker, I., 2006a. Investigation of Newtonian creep in polycrystalline ice.
999 *Philos. Mag. Lett.* 86(12), 763–771. doi: 10.1080/09500830601023787.
- 1000 Song, M., Cole, D.M., Baker, I. 2006b. An investigation of the effects of particles on creep of
1001 polycrystalline ice. *Scr. Mater.* 55, 91–94. doi: 10.1016/j.scriptamat.2006.03.029.

- 1002 Song, M., Baker, I., Cole, D.M., 2008. The effect of particles on creep rate and microstructures of
1003 granular ice. *J. Glaciol.* 54(186), 533–537. doi: doi:10.3189/002214308785836959.
- 1004 Srivastava, P.K., Mahajan, P., Satyawali, P.K., 2010. A constitutive law for the densification of
1005 polar firn. *Cold Reg. Sci. Technol.*, 60(2), 133-138.
- 1006 Theile, T., Lowe, H., Theile, T.C., Schneebeli, M., 2011. Simulating creep of snow based on
1007 microstructure and the anisotropic deformation of ice. *Acta Mater.* 59, 7104–7113. doi:
1008 10.1016/j.actamat.2011.07.065.
- 1009 Thomas, R.H., MacAyeal, D.R., Bentley, C.R., Clapp, J.L., 1980. The creep of ice, geothermal
1010 heat flow, and Roosevelt Island, Antarctica. *J. Glaciol.* 25, 47–60.
- 1011 Treverrow, A., Budd, W.F., Jacka, T.H., Warner, R.C., 2012. The tertiary creep of polycrystalline
1012 ice: experimental evidence for stress-dependent levels of strain-rate enhancement. *J. Glaciol.*
1013 58(208), 301–314. doi: 10.3189/2012JoG11J149.
- 1014 Vickers, W., Greenfield, P., 1968. The high temperature creep properties of compacted
1015 magnesium powder. *Journal of Nuclear Materials*, 27(1), 73-79.
- 1016 Wang, X., Baker, I., 2013. Observation of the Microstructural Evolution of Snow under Uniaxial
1017 Compression using X-ray Computed Micro-tomography, *J. Geophys. Res.*, 118, 1-12,
1018 doi.org/10.1002/2013JD020352.
- 1019 Weertman, J., 1983. Creep deformation of ice. *Annual Review Earth Planet Science*, 11, 215–240.
- 1020 Weertman, J., 1985. Unsolved problems of creep. *Nat.* 314(6008), 227.
- 1021 Wiese, M., Schneebeli, M., 2017. Snowbreeder 5: a Micro-CT device for measuring the
1022 snow-microstructure evolution under the simultaneous influence of a temperature gradient
1023 and compaction. *J. Glaciol.*, 63(238), 355–360, doi: 10.1017/jog.2016.143.